Origin of low proton-to-electron temperature ratio in the Earth's plasma sheet

E. E. Grigorenko (Space Research Institute of RAS, Moscow, Russia, elenagrigorenko2003@yandex.ru)

E. A. Kronberg, (Max Planck Institute for Solar System Research, Göttingen, Germany, kronberg@mps.mpg.de; Ludwig Maximilian University of Munich, Munich, Germany)

P. W. Daly (Max Planck Institute for Solar System Research, Göttingen, Germany, daly@mps.mpg.de)

N. Yu. Ganushkina (Finnish Meteorological Institute, Helsinki, Finland, natalia.ganushkina@fmi.fi; University of Michigan, Ann Arbor, MI, USA)

B. Lavraud (Institut de Recherche en Astrophysique et Planétologie, Université de Toulouse (UPS), France; Centre National de la Recherche Scientifique, UMR 5277, Toulouse, France, Benoit.Lavraud@irap.omp.eu)

J.- A. Sauvaud (Institut de Recherche en Astrophysique et Planétologie, Université de Toulouse (UPS), France; Centre National de la Recherche Scientifique, UMR 5277, Toulouse, France, Jean-Andre.Sauvaud@irap.omp.eu)

L. M. Zelenyi (Space Research Institute of RAS, Moscow, Russia, lzelenyi@iki.rssi.ru)

Abstract

We study the proton-to-electron temperature ratio (T_p/T_e) in the Plasma Sheet (PS) of the Earth's magnetotail using five years of Cluster observations (2001-2005). The PS intervals are searched within a region defined with $-19 < X \leq -7R_E$ and $|Y| < 15R_E$ (GSM) under the condition $|B_X| \leq 10$ nT. 160 PS crossings are identified. We find an average value of $<T_p/T_e> \sim 6.0$. However, in many

This is the author manuscript accepted for publication and has undergone full peer review but has not been through the copyediting, typesetting, pagination and proofreading process, which may lead to differences between this version and the Version of Record. Please cite this article as doi: 10.1002/2016JA022874

PS intervals T_p/T_e varies over a wide range from a few units to several tens of units. In 86 PS intervals the T_p/T_e decreases below 3.5. Generally the decreases of T_p/T_e are due to some increase of T_e while T_p either decreases or remains unchanged. In the majority of these intervals the T_p/T_e drops are observed during magnetotail dipolarizations. A superposed epoch analysis applied to these events shows that the minimum value of T_p/T_e is observed after the dipolarization onset during the "turbulent phase" of dipolarization, when a number of transient B_Z pulses is reduced, but the value of B_Z is still large and an intensification of wave activity is observed. The T_p/T_e drops and associated increases of T_e often coincides either with bursts of broad-band electrostatic emissions, which may include electron cyclotron harmonics (ECH), or with broad-band electromagnetic emission (EME) in a frequency range from proton plasma frequency (f_{pp}) and up to the electron gyrofrequency (f_{ce}). These findings show that the wave activity developing in the Current Sheet (CS) after dipolarization onset may play a role in the additional electron heating and the associated T_p/T_e decrease.

Key points

During dipolarizations transient drops of T_p/T_e below ~3.5 often coincide with wave bursts in the frequency range $f_{pp} \leq f \leq f_{ce}$

Generally the decreases of T_p/T_e are due to some increase of T_e while T_p either decreases or remains unchanged

Electron heating by ECH and EME with $f_{pp} \leq f \leq f_{ce}$ can be an additional mechanism affecting the T_p/T_e during dipolarizations.

1. Introduction

Thermal characteristics of the Plasma Sheet (PS) population reflect the energy dissipation processes operating either locally or at a remote location. The important parameter is the proton-to-electron temperature ratio T_p/T_e, which may influence the Current Sheet (CS) dynamics and

stability. There are several mechanisms of plasma heating in the Earth's magnetotail and they can operate in different ways for ions and electrons. Ions can be efficiently heated and accelerated in the course of their non-adiabatic interaction with a thin CS or in the vicinity of a magnetic reconnection X-line [e.g. *Ashour - Abdalla et al.,* 1993;1996 and references therein, *Hoshino et al.,* 1998], while electrons can be efficiently heated adiabatically in the course of gradient and curvature drifts in the reconnection pile-up region and by surfatron acceleration at the boundary [e.g. *Hoshino et al.*, 2001; 2005; *Imada et al.*, 2007; *Fu et al.*, 2013a], in the contracting and/or coalescing magnetic islands [e.g. *Drake et al*., 2006; *Oka et al.*, 2010], in dipolarization events [e.g. *Birn et al.,* 2013 and references therein] and in the course of their earthward convection by the convection electric field [*Lyons*, 1984].

The different efficiencies of the heating mechanisms affect the value of T_i/T_e. An important source of hot ion population in the near-Earth tail are bursty bulk flows (BBF), which transport the heated ion population from the distant acceleration sources to near Earth [e.g. *Angelopoulos et al.*, 1992; *Sergeev et al.*, 1996; *Ohtani et al.*, 2004; *Sharma et al.*, 2008]. During these periods electrons can experience adiabatic betatron and/or Fermi accelerations at the associated dipolarization fronts [e.g. *Fu et al.*, 2011, *Birn et al.*, 2013; 2014 and references therein]. These mechanisms are believed to be the major acceleration mechanisms for electrons. However, as it was shown in analytical simulations by *Zelenyi et al.* [1990] and in a recent MHD simulation of magnetotail reconnection, flow bursts and dipolarization by *Birn et a*l. [2013] ions, although non-adiabatic experience the similar acceleration as adiabatic electrons, at least, in the cases, when the spatial scale of magnetic field gradient exceeds an ion gyroradius and full orbit integration can be applied. This comes from the fact that in the presence of the magnetic field gradient and the dawn-dusk electric field the net energy gain of nonadiabatic ions is obtained at the last part of their orbits because of the difference

between the duskward and dawnward parts of the ion trajectory. Since this is also the essence of betatron mechanism the last generally should not affect the T_i/T_e ratio.

However, significant variations of T_i/T_e were reported in many studies using different instruments and different criteria for the plasma region selection. [e.g. *Baumjohann et al.*, 1989; *Kaufmann et al.*, 2005; *Artemyev et al.*, 2011; *Wang et al.*, 2012; *Runov et al.*, 2015]. *Baumjohann et al* [1989] by using the AMPTE/IRM data reported that the value of T_i/T_e ranges between ~5 and ~ 10 with an average value ~ 7.0. Similar values of T_i/T_e were obtained by *Kaufmann et al* [2005] using the Geotail data. For their analysis the authors used observations with $T_e \leq 11$ MK that, in some cases, may cause an overestimation of T_i/T_e.

Wang et al. [2012] used THEMIS observations to study statistically how T_i/T_e ratio changes spatially in the magnetosheath and in magnetotail and to identify the processes responsible for these changes. Authors showed that changes in T_i/T_e depend on the initial state of the PS, on the interplanetary magnetic field (IMF) direction and on AE index. It was demonstrated that during the periods of cool PS T_i/T_e varies between ~ 6 and 10. This value increases closer to the magnetotail flanks and during the periods of northward IMF. During the period of hot PS and high AE index T_i/T_e decreases and becomes ~ 2 – 5. Authors suggested that the lower values of T_i/T_e can be produced of non-adiabatic heating of electrons. For the near-Earth tail region (X > -10 R_E) authors reported a strong dawn-dusk asymmetry with very high T_i/T_e (~ 15 – 100) observed near the dusk flank and very low T_i/T_e (~ 1) registered near the dawn flank. Authors explained this feature by gradient drift of hot ions towards the dusk flank and of hot electrons - towards the dawn flank.

Runov et al. [2015] used THEMIS data to study average thermodynamic properties of the plasma in and around dipolarizing flux bundles (DFB) in the magnetotail at radial distances 5 < R <

25 R_E. To select the PS region authors used samples collected within $|B_X| < 15$ nT for $R < 12$ R_E and $|B_X| < 10$ nT for $R > 12$ R_E. They reported that for relatively cold ion populations ($T_i < 10$ keV) the average value of T_i/T_e is ~ 7, while for the hotter ion population and closer to the Earth (at $R < 12$ R_E) T_i/T_e decreases down to ~1.0. The analysis of 9 events with T_i/T_e ~1 showed that seven from them were detected near the dawn side of DFB. Authors explained the drop of T_i/T_e by the gradient drifts of ions and electrons in opposite directions, so that hotter electrons appear near the dawnward edge of DFB, while hot ions drift duskward.

Sergeev et al. [2015] using data from six tail seasons of THEMIS observations showed statistically that proton and electron temperature and pressure depend in a different ways on solar wind conditions and substorms. While the proton parameters are well correlated with the solar wind density, velocity and temperature, the behavior of electron temperature and pressure in the PS is mostly controlled by the substorm-related processes. Authors showed that during the periods of BBFs electrons experience a stronger heating than protons, so that T_i/T_e can occasionally drop down to ~ 1.

Strong variations of proton-to-electron temperature were reported in statistical sudy by *Artemyev et al.* [2011] based on 4-year of Cluster observations in the near-Earth magnetotail. Authors reported that the average value of T_p/T_e ~ 3.5 and it can occasionally decrease below 2.0. Authors used proton moments obtained by the Composition and Distribution Function Analyser (CODIF) [*Réme et al.*, 2001], which measures proton population in energy range below 40 keV. They found statistically that the dependence of T_p on T_e can be approximated by the power law function and showed that the higher values of T_e are observed during intervals of larger values of the ion and electron bulk velocities.

Summarizing the previous results one can conclude that the transient processes in the PS associated with the substorm related phenomena (magnetic dipolarizations, bursty bulk flows and so on) may affect electron population in much significant way than the ion one, and cause the decrease of T_p/T_e. In the present paper we study in detail the PS dynamics observed during the periods of low T_p/T_e ($\leq$ 3.5, the average value reported by *Artemyev et al.*, [2011]) in order to identify the additional nonadiabatic mechanisms which may affect electron and/or proton temperature and cause T_p/T_e decrease. For this purpose we study 5 years of Cluster observations in the PS of the near-Earth tail (-19 < $X \leq$ -7 R_E) using the $|B_X| \leq$ 10 nT as the PS selection criterion. To determine proton temperature we used both CODIF data and the observations provided by the 'Research with Adaptive Particle Imaging Detectors' (RAPID) [*Wilken et al.*, 2001] to avoid a possible underestimation of proton temperature and T_p/T_e value during hot PS periods.

The structure of the paper is as follows. In the next section we describe the data selection for the statistical analysis and present the statistical distribution of the average < T_p/T_e > value in the PS. In Section 3 we show one example from our data base in which a $T_p/T_e \sim 2.0$ was observed and discuss the associated PS dynamics. In Section 4 we present the statistical analysis to reveal at which phase of the PS dynamics the minimum of T_p/T_e is observed. In the last section we summarize our results and discuss the possible mechanisms responsible for the decrease of T_p/T_e in the near-Earth tail. In the Appendix we present the list of the PS intervals from our data base, in which $T_p/T_e \leq 3.5$ is observed and describe phenomena associated with the T_p/T_e decreases.

2. Data selection and statistical distribution of $<T_p/T_e>$

We have analyzed five years of Cluster observations in the near-Earth magnetotail in 2001-2005. The PS intervals were selected as the samples when $|B_X| \leq$ 10 nT within the region with -19 <

$X \leq$ -7 R_E and $|Y| <$ 15 R_E. The magnetic field data are obtained by the fluxgate magnetometer (FGM) [*Balogh et al*., 2001]. The electron moments are obtained by the Plasma Electron and Current Experiment (PEACE) [*Johnstone et al.*, 1997].

We used observations from Cluster-1 and Cluster-3 spacecraft (hereafter Cl-1 and Cl-3) and found in total 731961 PS samples (4s bins) observed in 160 intervals. The GSM coordinate system was used for orbit and magnetic field data. In Figure 1 we display the scatterplots of the selected PS samples in the (*YZ*) and (*XY*) planes.

For each PS sample the values of the proton and electron moments were obtained from the Cluster Science Archive and interpolated (a linear interpolation was used) to the magnetic field data. It is worth noting that during periods of strong ion heating the proton temperature and T_p/T_e value can be underestimated, because the ion energy approaches the upper energy threshold of the CODIF instrument, and, hence, only the low energy part of the high energy ion population is actually measured. Indeed in our data base in approximately 30 % of the PS crossings the energy corresponding to the peak of proton flux exceeded 20 keV. To avoid such bias we performed a visual analysis of the intervals with low values of T_p/T_e ($\leq$ 4.0). For those PS intervals, in which proton energy corresponding to the peak particle flux becomes $\geq$ 20 keV (~half of the value of the CODIF upper energy threshold), we calculate T_p using both CODIF and RAPID observations according to the method described by *Daly and Kronberg* [2015] and *Kronberg et al.* [2015]. By combining observations from the two Cluster instruments (CODFI and RAPID) we have found that the minimum trusted value of T_p/T_e is ~ 2.0.

A possible other bias could come from the entry of low T_p/T_e plasma populations (of solar wind origin) from the flanks during low solar wind Mach number [*Lavraud et al.*, 2009] or northward IMF B_Z period [*Fu et al*., 2012a].. In such instances a low T_p/T_e is observed in the

magnetosheath from overall lower particle heating, and of protons in particular, at the low Mach number bow shock. Subsequent entry of this low T_p/T_e through the magnetopause was observed [*Lavraud et al.*, 2009]. However, this does not appear to be a possible bias for the low T_p/T_e events from our data base, since they statistically correspond to more central PS intervals with typical high temperatures, so that the plasma seems heated by local magnetotail processes.

Figure 2a presents the statistical 2D distribution of the average values of $<T_p/T_e>$ in the (*XY*) plane within the region of interest. The $<T_p/T_e>$ were averaged within each $2R_E$ x $2R_E$ bin. To construct this distribution we use only those (*XY*) bins in which the number of data samples exceeded 10. The bins in which the number of data samples ≤ 10 are colored white. The majority of the other colored bins contains >100 data samples per bin.

The value of $<T_p/T_e>$ averaged over the whole region of study is ~ 6.0. The median value of the observed T_p/T_e is 4.5. Figure 2b displays the $<T_p/T_e>(R)$ profile integrated over all *Y* locations for a given *R* bin. One can see that the $<T_p/T_e>$ decreases towards the Earth from ~6.0 at R ~ 18 R_E to $<T_p/T_e>$ ~ 3.0 at R ~ 10 R_E, which is consistent with the previous results of T_i/T_e spatial behavior obtained by THEMIS observations [*Wang et al.*, 2012; *Runov et al.*, 2015] Unfortunately, magnetotail segments of Cluster orbits during the time period studied do not allow the detailed study of the radial distribution of the T_p/T_e in the PS within the midnight sector ($|Y| \leq 5$ R_E).

Figure 2c shows the $<T_p/T_e>(Y)$ profile integrated over all *R* locations for a given *Y*-bin. Within the R ~ 10 to 18 R_E no evident dawn-dusk asymmetry in the $<T_p/T_e>$ distribution is observed. There is an increase of T_p/T_e ~ 20.0 at Y ~ -14 R_E. Although there are many data samples (~ 1500) within the corresponding *Y* – bin, this was only a single PS crossing when very hot proton population was observed.

The absence of dawn-dusk asymmetry in the $<T_p/T_e>$ distribution obtained from our observations is opposite to the results by *Wang et al*. [2012], which reported a dawn-dusk asymmetry in the T_i/T_e distribution with the smallest values of T_i/T_e detected at the dawn flank. This discrepancy can be explained by different radial distances between our observations and those of *Wang et al*. The asymmetry reported by *Wang et al.* was observed closer to the Earth at $X > -6$ R_E. The authors suggested that the decrease of the T_i/T_e in the dawn flank and its increase in the dusk flank are associated with the gradient drifts of hot ions and electrons towards the dusk and dawn flanks respectively. Near the Earth this effect dominates. However, further downtail other mechanisms can smear out this asymmetry. In the following sections we discuss another possible mechanism which can contribute to the decrease of T_p/T_e in the PS.

Figure 2d presents a histogram of the occurrence frequency distribution of the T_p/T_e observed in the PS samples from our data base. It is seen that a wide range of the T_p/T_e is detected in the PS. The most frequently observed values are $3.0 \leq T_p/T_e < 5.0$. The the lower and upper quartiles are 4.0 and 5.5 respectively. There is also some fraction of the PS samples in which the $T_p/T_e < 3.0$ is observed. An example of such observations is presented in the next section.

3. Variations of the T_p/T_e and associated PS dynamics

It was mentioned above that the T_p/T_e value varies significantly in the PS and can occasionally drop down to ~ 2.0. Figure 3 shows an example of the PS crossing by Cl-1, in which such a phenomenon was observed. On 8.10.2001 between 13:20 and 15:50 UT Cluster was located in the magnetotail PS at [-15.7, 9.7, -0.2] R_E. During the interval of interest the energy corresponding to the peak electron flux is well below the upper energy threshold of the PEACE

instrument (see electron Energy-Time spectrogram in Figure3a). However, for protons the energy corresponding to the peak flux approaches to the upper energy threshold of the CODIF instrument (see Energy-Time spectrogram of protons in Figure 3b). Thus, to calculate T_p we used both CODIF and RAPID data.

From the time profiles of the T_p and T_e shown in Figure 3c it is seen that during this event there are periods when the temperatures of both species change in a similar way, so that T_p/T_e is roughly constant. Such changes of particle temperature without affecting the T_p/T_e value are most likely caused by the adiabatic mechanisms operating during magnetic dipolarizations and discussed before by e.g. *Zelenyi et al.,* [1990], *Fu et al.,* [2011], *Birn et al.,* [2013], *Runov et al.* [2015]. However, there are also periods when the T_p and T_e either change in an opposite way or their increase (or decrease) occurs with different speeds. This leads to the observed significant variations in T_p/T_e between ~ 20.0 and 2.0 (see Figure 3d). Such strong variations may indicate the importance of additional, possible, nonadiabatic mass-dependent mechanisms of particle heating. We may roughly select three periods when T_p/T_e becomes ≤ 3.5, which are marked as "I", "II" and "III" and by vertical dashed lines in Figure 3.

Between 13:20 and 15:50 UT several periods of magnetic dipolarization are observed. The first strong dipolarization starts around 14:03 UT with the positive jump ΔB_Z ~ 23 nT (see Figure 3f). After the onset the B_Z field remains larger than it was before the onset and fluctuating during ~ 0.5h. Five transient pulses of the B_Z field with the amplitudes 8 – 16 nT were observed within ~8 min after the onset. At the later phase of the dipolarization event (between 14:11 and 14:19 UT) only one pulse of the B_Z field was observed (at ~14:15 UT). During this later phase, which we will call below as the "turbulent" phase of dipolarization, the B_Z field remains still large and experiences

low-amplitude fluctuations along with the enhancement of wave activity in the frequency range up to electron gyrofrequency (f_{ce}) (see Figure 3g,h).

The first drop of T_p/T_e (period I) precedes the onset of dipolarization. During this period strong PS flapping is observed: the B_X field experiences fast variations between -15 nT and +20 nT, so that the Cluster periodically exits to the outer PS. Bursts of wave activity are observed in the electric and magnetic field wave spectra measured from 8 Hz to 4096 Hz by the Spatio-Temporal Analysis of Field Fluctuations (STAFF) experiment [*Cornilleau-Wehrlin* et al., 1997] and shown in Figure 3g,h. The time profiles of f_{ce}, proton plasma frequency (f_{pp}) and the lower hybrid frequency $f_{LH} = (f_{ce} \cdot f_{ci})^{1/2}$ are shown by white, magenta and black lines, respectively. The values of proton and electron temperatures experience variations and T_p/T_e ranges between ~10 and ~3.0. We do not discuss the period I in detail, since, because of the fast PS flapping it is difficult to link the T_p/T_e variations with specific processes in the central PS. We just mention briefly that during this period the broad-band electromagnetic emissions (EMEs) from 0.25 Hz to several tens of Hz ($\leq f_{pp}$) are observed. At higher frequencies (up to f_{ce}) the electrostatic emission is detected. The power of this emission increases in the outer part of the PS (in the region with $|B_X| > 10$ nT) and decreases in the central PS region (not shown). These fluctuations may represent the broad-band electrostatic noise (BEN), which is often observed in the PSBL and in the outer PS in the course of propagation of field-aligned beams [e.g. *Gurnet et al.*, 1976; *Matsumoto et al.*, 1994]. The study of these phenomena is beyond the scope of the present paper.

After the dipolarization onset, during period II, the strongest variations of T_p/T_e between 19.0 and 2.0 are observed. During this period Cluster was mainly located in the central PS ($|B_X| \leq 5$ nT). A zoom of Cl-1 observations during period II is shown in Figure 4. The absolute minimum of T_p/T_e

~ 2.0 was observed at 14:12:44 UT, i.e. after the observation of multiple B_Z pulses (see Figure 4e). Figure 4b shows the time profiles of parallel and perpendicular temperatures of protons (black line) and electrons (red lines). Since during this period the energy corresponding to the peak proton flux was well below the upper energy threshold of the CODIF instrument (see proton Energy-Time spectrogram in Figure 3b) we used the parallel and perpendicular proton temperatures calculated from the CODIF data.

In the beginning of the interval, between 14:10 – 14:10:45 UT, T_p/T_e experiences small variations around ~4.0 (see Figure 4e). From 14:10:45 UT T_p/T_e starts to decrease. Between 14:10:45 and 14:11:11:45 UT the decrease of T_p/T_e was due to the significant decrease of T_p and the increase of T_e. The decrease of T_p while electrons are being heated is a puzzling feature. *Zelenyi at al*. [1990] and *Birn et a*l. [2013] showed that the betatron mechanism of electron heating and non-adiabatic ion interaction with the CS in the presence of magnetic field gradient provide the similar energy gain for both plasma components. This condition can be broken if the characteristic spatial scale of magnetic field gradient becomes less than an ion gyroradius ρ. The observed anticorrelation between ΔT_p and ΔT_e may indicate on the existence of the small-scale ($\leq \rho_p$) magnetic gradients. In such case one can observe only that part of a proton orbit at which particle moves in the direction opposite to the electric field and losses its energy. Another possibility of the T_p decrease is the dissipation of their energy due to the interaction with low-frequency waves. Also the observed decrease of T_p can be due to the crossing of different plasma tubes populated by plasma coming from different sources. This puzzling feature deserves a further investigation.

Electrons are heated mainly by betatron mechanism [e.g. *Fu et al*., 2011; *Birn et al*., 2013; 2014]. But sometimes additional mechanisms may contribute to the observed variations of T_e. In Figure 4c we present the time profile of electron perpendicular temperature gain measured by

PEACE instrument at the *i*-th time moment: $\Delta T_{e\perp}(i) = T_{e\perp}(i) - T_{e\perp}(i-1)$ (it is shown by the red line) and the time profile of electron temperature gain expected from the betatron heating: $\Delta T_{e\_betatron} = T_{e\perp}(i-1) \cdot \frac{B(i)}{B(i-1)} - T_{e\perp}(i-1)$ (shown by the black line). One can see that there are time moments when $\Delta T_{e\perp}$ and $\Delta T_{e\_betatron}$ have opposite signs. At such moments additional mechanisms may contribute to the observed changes of $\Delta T_{e\perp}$.

In Figure 4d we show a power δB^2 of the magnetic field fluctuations integrated over the [f_{pp}, f_{ce}] frequency range. It is seen that the positive $\Delta T_{e\perp}$ are often observed at the moments of the δB^2 increase. The correlation coefficient between $\delta B^2(t)$ and $\Delta T_{e\perp}(t)$ $CC\sim 0.62$. As it was discussed by *Fu et al.* [2011; 2012a; 2014], the betatron heating of electrons increases their perpendicular anisotropy, which, in turn, can be a source for the whistler wave generation. For a few short intervals corresponding to the period of T_p/T_e decrease we tried to define a link between the changes in electron anisotropy and in the wave spectra. These intervals are marked as "1","2" and "3" in Figure 4.

Before the start of interval "1" at 14:11:11 UT the electron distribution was almost isotropic (see Figure 4b). At 14:11:11 UT the perpendicular anisotropy increases. The moment of $T_{e\perp}$ increase is marked in Figure 4b by the black arrow. Around this moment $\Delta T_{e\perp}$ and $\Delta T_{e\_betatron}$ variations have the opposite signs (Figure 4c). Thus, the betatron mechanism cannot be responsible for the observed increase of electron perpendicular temperature. In Figure 5 we show the energy distribution of 0^0,90^0 and 180^0 electrons measured at 14:11:11 – 14:11:19 UT along with the time series of 1s averaged spectra of the electric and magnetic field fluctuations observed by STAFF instrument just before and during the two-spin period.. One can see that just 1s before the appearance of the

perpendicular anisotropy the increase of electric field power localized near f_{ce} is detected. The ECH was observed during ~ 2s and then disappeared. Note that the observation of ECH after dipolarization onset was previously reported by *Zhou et al.* [2009]; *Zhang and Angelopoulos* [2014]. They demonstrated that these fluctuations can energize resonant electrons. The generation of the ECH can be due to the positive slope in 90^0 electron distribution observed in the energy range 0.2 – 1 keV at 14:11:03-14:11:11 UT (not shown) [e.g. *Zhou et al*., 2009]. We can assume that the ECH can contribute to the perpendicular electron heating and the increase of the perpendicular anisotropy.

Approximately 4s after the increase of $T_{e\perp}$ a bulge near f_{pp} appears both in the electric field and magnetic field power spectra. Figure 4i shows the direction of the Poynting flux of EME relative to the ambient magnetic field. It is seen that the broad-band EME consists of oblique wave modes in the low frequency range ($f \leq f_{pp}/2$), which may represent Alfven waves. The waves with $f \sim f_{pp}$ have their Poynting flux directed almost parallel to the ambient magnetic field. During this time Cl-1 was located mainly in the southern part of the central PS (see the time profile of B_X field in Figure 4h), so that the wave modes with $f \sim f_{pp}$ propagated outward from the neutral sheet. Such behavior is typical for whistler modes, which are often observed during magnetic dipolarizations and near a reconnection region [e.g. *Petkaki at al.* 2006; *Le Contel et al.*, 2009; *Viberg et al*., 2014, *Fu et al*., 2014]. Thus, we may assume that the generation of ECH before the start of interval "1" caused the perpendicular heating of electrons in a finite energy range and the increase of perpendicular anisotropy. The last, in turn, can be a source for the whistler wave generation with $f \sim f_{pp}$.

After 14:11:19 UT the perpendicular anisotropy in electron distribution decreases. By this time the ECH disappeared and the magnetic field power corresponding to the bulge near f_{pp} reduced

also. The next increase of $T_{e\perp}$ is observed during interval "2" at ~ 14:11:30 UT (this moment is marked by the second black arrow in Figure 4b). Similarly to interval "1" the variations of $\Delta T_{e\perp}(t)$ and $\Delta T_{e\_betatron}(t)$ observed during this interval do not correlate. Again the increase of $T_{e\perp}$ is preceded by the observation of ECH at 14:11:25 – 14:11:30 UT (see the corresponding spectra in Figure 5). At 14:11:30 UT a bulge near f_{pp} appears in the magnetic and electric field power spectra. This bulge then spreads to the higher frequency range up to f_{ce} denoting the generation of the broad-band whistler EME. This emission disappears rapidly (compare 1s-averaged spectra at 14:11:31 and at 14:11:35 UT in Figure 5). Comparing the electron distributions measured during the periods "1" and "2" one can see that in the last period the increase of phase space density of 90^0 electrons expanded to the lower energy range. Similarly to the previous interval we may assume that the ECH contribute to the perpendicular heating of electrons and to the increase of perpendicular anisotropy. The last can be a source for generation of whistler waves. Possibly the process of electron interaction with the waves had nonlinear character, which manifests in expansion of the EME in higher frequency range up to f_{ce} and its fast damping due to the absorption of wave energy by resonant electrons.

The absolute minimum of $T_p/T_e \sim 2.0$ was observed during interval "3" at 14:12:44 UT (this moment marked by the blue arrow in Figure 4b). Around this moment both T_p and T_e increased but T_e experienced the faster increase. The minimum of T_p/T_e coincides with the positive variation of $T_{e\perp}$ while the corresponding variation of $\Delta T_{e\_betatron}$ is negative. Again we may assume that other additional mechanism contributed to the electron heating.

During interval "3" the most intense wave emissions were detected. A bulge near f_{pp} in the spectra of the magnetic and electric field fluctuations was observed permanently from ~ 14:12:20 UT and until 14:12:40 UT. This bulge can be produced by whistler waves propagating almost along the magnetic field and outward the neutral sheet (see Figure 4f,i). These waves can be generated due to the presence of electron perpendicular anisotropy (Figure 4b). Another possible source for the waves can be related to plasma density and magnetic field gradients [e.g. *Le Contel et al.*, 2009], which can be observed near the leading edge of a high-speed bulk flow. Indeed the *X*-component of proton velocity started to increase in the beginning of interval "3" and reached its maximum value V_X ~ 500 km/s by the end of this interval (at 14:13:30 UT, see Figure 4a).

In Figure 5 we show the electron distribution measured around the T_p/T_e minimum at 14:12:44 – 14:13:40 UT and 1s-averaged wave spectra observed during 5s interval preceding the detection of this distribution. In comparison to the previous intervals the increase of phase space density was observed for 90^0 electrons in the wider energy range: from a few hundreds of eV and up to 20 keV. In the STAFF spectra the wave power in the [f_{pp},f_{ce}] range increased at 14:12:40 UT and it was observed until 14:12:43 UT (see the corresponding spectra in Figure 5). As in the previous periods the EME most likely represents the broad-band whistler EME and consists of wave modes with $f \sim f_{pp}$ propagating almost along the magnetic field outward the CS and the oblique waves with $f_{pp} < f \leq f_{ce}$. It is worth noting that the integral energy density of the EME was of the order of the observed ΔnkT_e (not shown). Thus we may assume that the EME can contribute to the electron heating observed during the first half of interval "3" when $\Delta T_{e\perp}$ and $\Delta T_{e\_betatron}$ .anticorrelated.

The wave energy dissipation just 1s before the minimum of T_p/T_e is confirmed by the significant change in the spectral slopes of the electric and magnetic field fluctuations. Indeed the

spectral indexes γ calculated for the electric and magnetic field power in the frequency range between the frequency of the bulge (~ f_{pp}) and f_{ce} changes from γ_E ~ -1.7 and γ_B ~ -2.4 in the beginning of interval "3" to γ_E ~ -6.5 and γ_B ~ -7.0 just before the T_p/T_e minimum observation. We may suggest that the changes in spectra near f_{ce} can be caused by the absorption of the wave energy by resonant electrons leading to their perpendicular heating.

In the rest part of interval "3' the periodic increases and damping of the broad-band whistler EME repeated. At the end of interval "3", when the maximum of the plasma bulk flow was observed a good correlation between $\Delta T_{e\perp}$ and $\Delta T_{e\_betatron}$ took place. Indeed, the last pronounced increase of $T_{e\perp}$ is due to the betatron heating since $\Delta T_{e\perp} \sim \Delta T_{e\_betatron}$.(Figure 4b,c).

Coming back to the analysis of the PS dynamics between 13:20 nd 15:40 UT one can see that the last decrease of T_p/T_e down to $\leq$ 4.0 was observed during the interval III between 14:57 and 15:27 UT (see Figure 3). The T_p/T_e decrease was due to the decrease of T_p and increase of T_e taking place just before the start of the interval. As in period II the exact mechanism responsible for T_p decrease is unknown. Before the start of interval III a dipolarization front was observed between 14:50 and 14:56:30 UT. Thus the observed electron heating in the beginning of interval III was produced by betatron mechanism [e.g. *Fu et a*l., 2011]. For protons we may assume that the observed decrease of their temperature can be related with the above mentioned effect of a finite spatial scale of the region of magnetic gradient.

The next magnetic dipolarization started around 14:57 UT. The B_Z field reached its maximum value ~ 24 nT at 15:05:39 UT. Two B_Z pulses were detected within ~ 9 min after the onset at ~15:03:20 UT and at ~15:05:39 UT. After the last pulse, which corresponds to the absolute

maximum value of the B_Z field reached in this event, the B_Z remains large and fluctuates with the smaller amplitude until ~15:14:30 UT. This period can be referred to the "turbulent" phase of dipolarization. The fluctuations of T_p/T_e observed during the "turbulent" phase and until the end of the dipolarization (at ~ 15:27 UT) are hardly related to the gradient effects, since no B_Z pulses are observed during this time. Within this period the broad-band electrostatic emissions and ECH are detected by the STAFF instrument. In this event the appearance of electron cyclotron fluctuations coincides with the local increase of T_e and decrease of T_p/T_e (this moment is shown by black arrow in Figure 3). At this time electron anisotropy (Figure 3e) also decreases to 1.0, suggesting the pitch angle scattering of electrons.

Our observations show that in the course of magnetic dipolarization nonadiabatic mechanisms related to wave-particle interactions may contribute to electron heating and the decrease of T_p/T_e. Electrostatic broad-band emissions with ECH and EME with frequencies up to f_{ce} may resonantly interact with electrons and cause their energization. In the next session we present the statistical analysis of the PS dynamics during the periods when the T_p/T_e became ≤ 3.5 and show that the majority of such events from our data base are observed after dipolarization onset, when the B_Z field is still large and enhancements of in EME and electrostatic fluctuations near f_{ce} are observed.

4. Statistical analysis of the T_p/T_e in the PS of the near-Earth tail.

We analyzed 160 intervals of the PS crossings by Cluster in 2001-2005 time period. In 86 PS intervals (~54 %) strong variations and drops of $T_p/T_e \leq 3.5$ were observed. In the majority of these cases (in 85 intervals) the drops of T_p/T_e were detected during magnetic dipolarizations. The majority of dipolarization events in our data base does not represent the isolated earthward

propagating dipolarization fronts but can be rather referred to the "final" dipolarization events discussed by *Nakamura et al.* [2009], which can be generated in the near-Earth tail due to the flux pileup. Indeed, the magnetic dipolarizations from our data base represent a prolonged enhancements of the positive B_Z field (up to ~ 10 - 30 nT) having a duration from a few tens of minutes and up to a few hours (see Table 1 in the Appendix). In the majority of cases the onset of these events and the following general growth of the B_Z field are followed by multiple transient pulses of the B_Z field, which are generally observed during the first 10 min after the onset and cease at the later phase of the dipolarization. In all these events, except one, the bunches of wave activity in the frequency range up to f_{ce} and higher were detected by the STAFF experiment simultaneously with the T_p/T_e decreases.

In Table1 of the Appendix we listed these PS intervals containing the T_p/T_e drops below 3.5 and the simultaneous STAFF observations of wave activity. In the majority of these cases the decreases of T_p/T_e were associated either with the broad-band EME or electrostatic emissions in the frequency range up to f_{ce}, which may heat electrons in the course of their resonant interaction with the wave modes near f_{ce}. In many cases ECH might also contribute to electron heating and to the corresponding T_p/T_e decrease.

In order to reveal statistically at which phase of magnetic dipolarization and under which conditions the T_p/T_e decreases we apply a superposed epoch analysis to the PS intervals listed in Table 1. The epoch analysis was applied to the following parameters: B_Z, T_p/T_e, T_p, T_e, the X-component of proton bulk velocity (V_X), plasma β, AE index and the electric and magnetic field wave power $\delta|E|^2(t)$ and $\delta(|B|^2(t)$ integrated within the frequency range [f_{pp}, f_{ce}]. For each event the B_Z field was normalized to the maximum value of the B_Z observed in a given event: $B_Z^*(t) = B_Z(t)/B_Z^{max}$.

As the epoch time (t = 0) we use the dipolarization onset for each event similarly to the previous study by e.g. *Fu et al.*, [2012b]. But in our data base the majority of cases represent rather complicated events with a multiple dipolarization pulses overlapped onto the general prolonged growth of the B_Z field (see, for example, the dipolarization event observed between 14:03 and 14:35 UT in Figure 3). To choose the onset (the epoch) time we use one of the following criteria. For the strong dipolarizations, in which the B_Z^{max} > 10 nT, the epoch time is chosen as the moment of the first B_Z increase with the amplitude $\Delta B_Z = B_{Zi} - B_{Z0} > 5$ nT, where B_{Zi} is the value of the B_Z increase and B_{Z0} is the value of the B_Z field averaged for 1 min before the increase. For a few week dipolarizations from our data base with the $B_Z^{max} \leq 10$ nT we choose the onset time as the moment of the first positive B_Z increase with $\Delta B_Z \geq 0.5 B_Z^{max}$. In the epoch analysis we also include data up to 15 min before the onset.

In some dipolarization events the B_Z field can transiently decrease after the onset and increase again within ten(s) of seconds denoting the presence of transient dipolarization pulse(s). We consider a variation of the B_Z field observed after the onset as the B_Z pulse if $\Delta B_Z > 5$ nT and $\Delta B_Z/B_{Z0} > 0.5$, where ΔB_Z is the difference between the peak value of B_Z in the pulse and the value B_{Z0} observed just before the pulse. It is worth noting that in all events from our data base the value of B_Z field observed after the onset and between the dipolarization pulses does not decrease below its initial level registered before the dipolarization onset. Thus, even in the presence of multiple B_Z pulses detected after the onset, the average B_Z field experiences a gradual growth up to the B_Z^{max}, which in some events may last during tens of minutes.

Figure 6 shows the resulting epoch profiles. In order to demonstrate the spread of data used for the epoch analysis we present in the corresponding panels of Figure 6 the scatterplots of low and upper quartiles displayed by grey dots. The zero epoch t = 0 corresponding to dipolarization onset

in each event is marked by the red vertical line. Along with the epoch profile of the B_Z*(t) we show two histograms of the distribution of the average (displayed by the red dotted line) and of the mean (displayed by the sold red line) number of the transient B_Z pulses detected within each 10-min bin after the onset of dipolarization events from our data base. It is seen that the maximum number of the B_Z pulses is observed within a first 10 min after the onset. After this time the mean value of the B_Z pulses calculated for the subsequent time bins is zero and the average value of the B_Z pulses is 1.0 within the next three 10-min bins and, then, becomes zero. Thus, following ~10 min after the onset a number of transient B_Z pulses decreased by ≥50%, while the value of B_Z still remains large and experiences low-amplitude fluctuations. During this period the increase of wave activity in [f_{pp},f_{ce}] range is observed. We mark this period by blue horizontal line in Figure 6 and call it as the "turbulent" phase of dipolarization.

The epoch profile of [T_p/T_e](t) experiences strong variations around dipolarization onset when the earthward and reflected high-speed flows are observed. It is worth noting that the [T_p/T_e](t) epoch profile represents an averaged tendency of how T_p/T_e changes and its single variations (e.g. drops) are smeared. Plasma β experienced strong fluctuations from a few to hundred units around and just after the onset denoting the presence of density gradients. The epoch profiles of $T_p(t)$ and $T_e(t)$ change more or less synchronously that is consistent with the previous results reporting the increase of electron temperature with the ion temperature [e.g. *Baumjohan et al.*; 1989; *Artemyev et al*. 2011]. However electron temperature increases faster and reaches its maximum earlier than proton one. The intense electron heating is observed around and after the onset and during the period of fast bulk flow and the AE maximum This confirms the importance of substorm related processes in electron heating reported earlier by *Sergeev et al*. [2015]. The epoch profile of $T_e(t)$ also shows that the maximum of electron temperature is prolonged in time and the

"plateau" of large $T_e(t)$ is observed during the first half of the "turbulent" phase of dipolarization, when the intensification of wave activity in high-frequency range (up to f_{ce}) are detected.

Our epoch analysis does not show the correlations between $[T_p/T_e](t)$ and bulk flows. The maximum of V_X coincides with the dipolarization onset as it was observed before in numerous studies [e.g. *Nakamura et al.*, 2002]. Just after the onset, the positive and negative variations of V_X are observed denoting the registration of the reflected/diversed flows. During this time $[T_p/T_e](t)$ fluctuates mainly due to T_p fluctuations. While dipolarization proceeds the $V_X(t)$ decreases close to zero. This does not mean that flow bursts are not observed during this time. The small V_X may denote the superposition of the earthward and reflected flows and/or flow braking. At this later ("turbulent") stage of dipolarization the increase of wave activity in $[f_{pp},f_{ce}]$ range is observed and it roughly coincides with the decrease of $[T_p/T_e](t)$ to the epoch minimum value.

This we may suggest that the minimum of $[T_p/T_e](t)$ is observed during the "turbulent" phase of dipolarization when the B_Z field is still large and the wave activity is enhanced. This suggests that electron interaction with the high frequency electrostatic and EME can be an additional mechanism providing local electron heating and affecting T_p/T_e during magnetic dipolarizations.

5. Discussion and Conclusion

In order to identify the PS processes which may affect electron and/or proton temperature and cause the decrease of T_p/T_e we have studied 5 years of Cluster observations in the near-Earth tail at $-19 < X \leq -7$ R_E and $|Y| < 15$ R_E by using the $|B_X| \leq 10$ nT as the criterion for PS selection. We have found and analyzed 160 intervals of PS crossings by Cluster. To avoid underestimation of T_p for the hot PS intervals, when the energy corresponding to the peak of proton flux exceeded 20 keV.(~ 30 % of the PS crossings in our data base), we calculate T_p using both CODIF and RAPID

observations [*Daly and Kronberg* [2015] and *Kronberg et al.* [2015]. Below we summarize our main results:

1. The value of T_p/T_e averaged over the whole region of the PS under study is ~ 6.0. This result is more or less in agreement with earlier results obtained from the observations by other space missions [e.g. *Baumjohann et al.*, 1989; *Kaufmann et al.*, 2005]. However, our estimation of the average value of T_p/T_e is larger than the one obtained in statistical study of Cluster observations by *Artemyev et al.* [2011]. According to their results the $<T_p/T_e>$ ~ 3.5. We explain this discrepancy by T_p calculation using both CODIF and RAPID observations during hot PS intervals while *Artemyev et a*l. [2011] used only CODIF data.

2. The T_p/T_e value decreases towards the Earth. from ~6.0 at R ~ 18 R_E to $<T_p/T_e>$ ~ 3.0 at R ~ 10 R_E, that is consistent with the previous results of T_i/T_e spatial behavior obtained by THEMIS observations [*Wang et al.*, 2012; *Runov et al.*, 2015]. Within the radial distances -9 to -19 R_E no evident dawn–dusk asymmetry in the $<T_p/T_e>$ distribution is observed.

3. Within a single PS interval the value of T_p/T_e may fluctuate in a wide range from a few units to several tens of units. According to our observations the minimum trusted value (from instrument limitations of Cluster) of T_p/T_e in the PS is ~ 2.0. The decreases of T_p/T_e below 3.5 (the average estimation obtained by *Artemyev et al.* [2011]) were detected in 86 PS intervals from our data base. In the majority of these cases (in 85 intervals) the drops of T_p/T_e were observed during magnetic dipolarizations.

4. The superposed epoch analysis applied to the dipolarization events in which decreases of $T_p/T_e \leq 3.5$ were observed in the PS shows that the T_p/T_e experiences strong variations around the dipolarization onset and decreases after the onset, during the "turbulent" phase of dipolarization, when the B_Z field in the CS is still large. The time interval of T_p/T_e drop below 3.5 coincides with

the enhancement of electric and magnetic field wave power in [f_{pp}, f_{ce}] frequency range. This denotes that the high frequency electrostatic and EME may play some role in electron heating and T_p/T_e decrease during magnetic dipolarizations.

Before discussing the results we would like to note that one should be very careful with the evaluation of the T_p/T_e value. The upper energy threshold (40 keV) of the CODIF instrument may result in underestimation of T_p and T_p/T_e values during active PS periods, when bursty bulk flows, dipolarization fronts and other perturbations are observed [e.g. *Angelopoulos et al.* 1992, *Runov et al.*, 2009]. For such periods the use of only CODIF observations may give values as low as $T_p/T_e \leq 1.0$. The visual examination of proton energy-time spectrograms showed that such low values are indeed mostly due to the unusually strong proton heating (with limitations owing to the CODIF upper energy threshold). Using RAPID measurements along with the CODIF data allowed us to obtain the reliable minimum value of the $T_p/T_e \sim 2.0$ for the PS intervals from our data base.

In almost all intervals from our database the decreases of T_p/T_e below 3.5 were detected in the PS during magnetic dipolarizations. The magnetic dipolarizations may represent earthward propagating fronts, which are generated by a downtail reconnection [e.g. *Sitnov et al*., 2009; *Fu et al.*, 2013]. Or they can be related with the CS reduction/disruption either due to the development of CS instabilities [*Lui* 2004 and references therein] or in response to fast flow braking [e.g. *Sergeev et al.*, 2012 and references therein]. *Nakamura et al.* [2009] classified such events as the "final" dipolarization due to the flux pileup. The evolution of these events in time and space can be complicated and include multiple transient dipolarizations around and after the onset.

Many observations and simulations reported significant electron heating at and behind dipolarization fronts by betatron and Fermi mechanisms [e.g. *Fu et al.*, 2011; *Brin et al.*, 2013; *Birn et al.*, 2014 and references therein]. However, as it was shown in theoretical paper by *Zelenyi et a*l.

[1990] and in simulations by *Birn et al.* [2013], ions, although nonadiabatic, undergo the similar energization as electrons. Thus generally these major mechanisms of plasma heating hardly affect the T_p/T_e.

Artemyev et al. [2011] and *Wang et al.* [2012] proved statistically that the thermal characteristics of electron population and T_p/T_e value depend on the background state of the PS and generally T_e is higher and T_p/T_e is lower in hot PS. *Artemyev et al*. [2011] also demonstrated that T_e increases during the period of high-speed plasma flows. *Sergeev et al.* [2015] showed a preferential heating of electrons and drop of T_i/T_e during the periods of BBFs.

Our epoch superposition analysis showed that $T_p(t)$ and $T_e(t)$ change more or less synchronously in the course of magnetic dipolarization which is consistent with results by *Artemyev et al*. [2011]. However at the onset and just after the onset the $T_e(t)$ increases more rapidly than $T_p(t)$. The intense electron heating coincides with the increase of the bulk V_X velocity at the dipolarization onset and with the increase of AE. This result is in agreement with the conclusion made by *Sergeev et al*. [2015] that the thermal characteristics of electrons are affected stronger than ion ones during substorm-related processes.

However the minimum of the epoch profile of $[T_p/T_e](t)$ is observed after the dipolarization onset during the "turbulent phase" of dipolarization when the B_Z is still large and the intensification of wave activity in $[f_{pp},f_{ce}]$ frequency range is observed. First of all we would like to check how instantaneous values of T_p and T_e changes near the absolute minimum of T_p/T_e observed in the PS intervals with $T_p/T_e \leq 3.5$. In Figure 7 we present a scatterplot of $\Delta T_e(i) = T_e(i)-T_e(i\text{-}1)$ versus the corresponding $\Delta Tp(i)$ calculated for each PS interval from our data base at the i-th time moment at which the absolute minimum of T_p/T_e was observed. It is seen that in majority of cases form our data base the minimum of T_p/T_e is reached due to the T_e increase and T_p decrease and generally the

decrease of T_p is larger than the corresponding increase of T_e. Such anticorrelation in T_p and T_e changes is a puzzling feature. As it was mentioned before, under the presence of magnetic field gradient and the dawn-dusk electric field the adiabatic electrons, in the course of their betatron heating, and non-adiabatic ions, in the course of their nonadiabatic motion in the CS, obtain the similar energy gain. The opposite signs of temperature changes observed for protons and electrons can be related to some kinetic effects of proton dynamics in the CS. *Birn et al* [2014] mentioned the importance of micro-instabilities operating at different kinetic scales which may affect ions and electrons at different ways. Another possibility is the presence of small-scale (less than proton gyroradius) magnetic gradients. In such case the full orbit integration is not applied and an observer can detect ions passing only that part of their orbits, at which they lose energy due to the motion antiparallel to the electric field. Also the transient decreases of T_p can be due to the spacecraft crossings of different plasma tubes connected with different sources. The exact mechanism responsible for the transient T_p decreases in the course of magnetic dipolarization is an open question which deserves farther investigation.

The analysis of STAFF observations of the electric and magnetic flied fluctuations in the frequency range from 8 Hz to 4096 Hz permitted the identification of several wave modes, which generation coincides with the T_p/T_e decreases. These modes are listed in Table 1 for each PS interval from our data base when the drops of $T_p/T_e \leq 3.5$ were observed (see the Appendix).

In the majority of cases the decreases of T_p/T_e coincide either with the observations of broadband EME or broadband electrostatic emissions. The last includes ECH in ~ 50% of events. The observations of these wave modes during magnetic dipolarizations were reported in previous studies [e.g. *Le Contel et al.*, 2009; *Deng et al.*, 2010, *Hwang et al.*, 2011, *Zhou et al*. 2009; *Fu et*

al., 2014; *Zhang and Angelopoulos*, 2014]. The broad-band EME comprise from the whistler waves in the frequency range $f \leq f_{pp}$, which propagate outward from the CS almost parallel to the magnetic field and oblique whistler waves in the higher frequency range $f_{pp} < f \leq f_{ce}$. For higher frequency modes we observed an increase of the spectral index, $|\alpha_E|$, denoting the significant reduction of the electric field power at frequencies closer to f_{ce}. This may indicate energy transfer from the wave to resonant electrons.

Khotyaintsev et al. [2011] discussed the processes of wave-particle interaction in the flow braking region and showed that whistler-mode waves can efficiently scatter electrons in pitch-angles and, thus, increase the efficiency of betatron acceleration for some part of electron distribution. They also demonstrated that the particle interaction with whistler modes limits the electron anisotropy caused by the betatron acceleration at lower energies, so that the resulting distribution has limited anisotropy below ~ 2 keV, and is more anisotropic at higher energies. Our analysis of electron pitch angle distributions presented in Section 3 showed similar features for the periods of the T_p/T_e drops associated with the ECH and broad-band EME. We observe electron pitch-angle scattering in the energy range below ~500 eV and perpendicular anisotropy at energies from ~ 500 eV and up to several keV. Also, a pronounced flat-top electron distribution feature was observed for 90^0 pitch angle electrons in the energy range 0.1 – 3 keV, suggesting perpendicular electron heating.

The possibility of electron energization and scattering by ECH was discussed before by, e.g. *Farrell et al.* [2003] and *Zhou et al.* [2009]. Our analyses also showed that in many events the observation of broadband electrostatic fluctuations and electron cyclotron waves coincides with a

local increase of T_e and a decrease of T_p/T_e. At such times the electron anisotropy $T_{e\|}/T_{e\perp}$ also decreases to 1.0, suggesting efficient electron pitch angle scatterings.

However it is rather difficult to reveal cause-and-effect relation between the generation of waves, kinetic effects in particle distributions and particle energization. As it was discussed by *Fu et al.* [2011; 2012a; 2014], the perpendicular anisotropy of electron distributions appeared due to the betatron heating can be a source for wave generation. However the generated waves may, in turn, interact with the resonant electrons, so that at the later stage this process can become nonlinear. It is worth noting also that the particle anisotropy is not the only source of whistler waves. They can be generated also due to the presence of plasma density gradients and magnetic field gradients [e.g. *Le Contel et al.*, 2009 and references therein] which are formed in the course of dipolarizations. Propagating through the background plasma these waves can interact with the ambient electron population and cause its heating.

Our analysis presented in Section 3 showed that during some intervals of T_p/T_e decrease the periodical enhancement and damping of ECH and EME emissions in frequency range [f_{pp}, f_{ce}] are observed in spite of the almost permanent presence of the perpendicular anisotropy in electron distributions. Also it was shown that the increases of wave power in [f_{pp}, f_{ce}] range more or less correlate with the local increases of electron temperature ΔT_e (see Figure 4c,d). The strong increase of spectral index γ observed in the spectra of electric and magnetic field fluctuations in frequency range [f_{pp}, f_{ce}] range just before the minimum of T_p/T_e (see Figure 5) confirms the possibility of energy exchenge between the waves and resonant electrons.

In Figure 8 we present the scatterplots of T_e (and T_p/T_e) versus the power of magnetic and electric field fluctuations δB^2, δE^2 integrated in [f_{pp},f_{ce}] frequency range for all time moments within

the PS intervals in which $T_p/T_e \leq 3.5$ was observed. Although data points are rather scattered there is a tendency to observe larger T_e with the increase of the fluctuations power. This tendency is more clearly observed for the electric field fluctuations, which may indicate on the role of high-frequency electrostatic emission in the electron heating. For T_p/T_e there is a tendency to observe lower values for the higher power of fluctuations. Again this tendency is more clearly observed for the electric field fluctuations.

Summarizing our results we may conclude that the processes of electron interactions with the ECH and EME emissions in $[f_{pp},f_{ce}]$ frequency range may play some role and provide some heating of electrons additionally to the major energization mechanisms like betatron and/or Fermi acceleration. Which mechanisms are responsible for the simultaneously observed T_p decrease during the periods of low T_p/T_e is still an open question and requires farther studies. It is worth noting that the changes in T_p/T_e and the related changes in particle velocity distribution functions may, in turn, affect the CS dynamics and the development of plasma instabilities. These problems deserve special theoretical and modeling studies, which may shed new lights on CS dynamics during magnetic dipolarizations.

Appendix

In Table 1 we list all the PS intervals when the $T_p/T_e \leq 3.5$ was observed. In the majority of these cases the decrease in T_p/T_e was registered during magnetic dipolarizations. The analysis of STAFF observations of the electric and magnetic flied fluctuations in the frequency range from 8 Hz to 4096 Hz permitted the identification of wave modes, observed in the PS simultaneously with the T_p/T_e decrease below 3.5. These modes are also listed in the Table 1.

Table 1. A list of the PS intervals when the $T_p/T_e \leq 3.5$ is observed

Time Interval	Magnetic dipolarization	Wave activity
22.07.01. 12:17 – 17:00 UT	yes	broadband EME ($f \leq f_{ce}$), whistler waves
26.07.01. 17:17 – 17:59 UT	yes	broadband EME ($f \leq f_{ce}$), whistler waves
26.07.01. 20:42 – 24:00 UT	yes	broadband electrostatic fluctuations ($f \leq f_{ce}$), electron cyclotron waves
27.07.01. 03:44 – 07:00 UT	yes	broadband electrostatic fluctuations ($f \leq f_{ce}$), whistler waves ($f \leq f_{pp}$)
27.07.01. 08:38 – 10:37 UT	yes	broadband electrostatic fluctuations ($f \leq f_{ce}$), electron cyclotron waves
31.07.01. 18:00 – 21:37 UT	yes	broadband EME ($f \leq f_{ce}$), electron cyclotron waves, whistler waves
08.08.01. 02:05 – 06:00 UT	yes	broadband electrostatic fluctuations ($f \leq f_{ce}$), electron cyclotron waves
12.08.01. 18:05 – 19:00 UT	yes	broadband EME ($f \leq f_{ce}$), whistler waves
15.08.01. 01:47 – 02:15 UT	yes	broadband electrostatic fluctuations ($f \leq f_{ce}$)
15.08.01. 05:33 – 07:40 UT	yes	broadband electrostatic fluctuations ($f \leq f_{ce}$)
15.08.01. 08:03 – 10:11 UT	yes	broadband EME ($f \leq f_{ce}$), electron cyclotron waves
22.08.01. 10:04 – 10:26 UT	yes	broadband electrostatic fluctuations ($f \leq f_{ce}$)
27.08.01. 04:15 – 05:50 UT	yes	broadband EME ($f \leq f_{ce}$), whistler waves, electron cyclotron waves
29.08.01. 11:23 – 12:36 UT	yes	broadband electrostatic fluctuations ($f \leq f_{ce}$)
07.09.01. 21:56 – 22:10 UT	yes	broadband electrostatic and EME ($f \leq f_{ce}$)
12.09.01. 13:15 – 13:45 UT	yes	broadband electrostatic and EME ($f \leq f_{ce}$)
15.09.01. 00:40 – 01:30 UT	yes	broadband electrostatic and EME ($f \leq f_{ce}$)
17.09.01. 08:14 – 10:07 UT	yes	broadband electrostatic ($f \leq f_{ce}$) and electron cyclotron waves
01.10.01. 10:18 – 11:00 UT	yes	broadband EME ($f \leq f_{ce}$), whistler waves, electron cyclotron waves
01.10.01. 12:54 – 13:41 UT	yes	broadband EME ($f \leq f_{ce}$), whistler waves, electron cyclotron waves
08.10.01. 14:03 – 14:35 UT	yes	broadband EME ($f \leq f_{ce}$), whistler waves
08.10.01. 14:57 – 15:27 UT	yes	broadband electrostatic fluctuations, electron cyclotron waves
11.10.01. 03:37 – 05:30 UT	yes	broadband electrostatic and EME ($f \leq f_{ce}$), whistler waves
20.10.01. 10:47 – 13:05 UT	yes	broadband electrostatic ($f \leq f_{ce}$) and electron

		cyclotron waves
21.07.02. 03:40 - 05:00 UT	yes	broadband electrostatic waves ($f \leq f_{ce}$)
21.07.02. 09:42 – 13:03 UT	yes	broadband EME ($f \leq f_{ce}$), whistler waves, electron cyclotron waves
21.07.02. 13:48 – 14:51 UT	yes	broadband electrostatic waves ($f \leq f_{ce}$), whistler waves, electron cyclotron waves
25.07.02. 22:26 – 23:58 UT	yes	broadband electrostatic ($f \leq f_{ce}$) and electron cyclotron waves
26.07.02. 04:17 – 08:00 UT	yes	broadband electrostatic ($f \leq f_{ce}$) and electron cyclotron waves
30.07.02. 17:53 - 19:05 UT	yes	broadband electrostatic waves ($f \leq f_{ce}$)
10.10.02. 01:59 – 02:22 UT	yes	broadband electrostatic waves ($f \leq f_{ce}$)
14.10.02. 12:20 – 14:10 UT	yes	broadband electrostatic waves ($f \leq f_{ce}$), electron cyclotron waves
14.10.02. 17:49 – 22:00 UT	yes	broadband electrostatic waves ($f \leq f_{ce}$), electron cyclotron waves
26.10.02. 07:03 – 08:22 UT	yes	broadband electrostatic waves ($f \leq f_{ce}$)
20.07.03. 00:19 – 02:06 UT	yes	broadband EME ($f \leq f_{ce}$), whistler waves, electron cyclotron waves
20.07.03. 03:06 – 05:37 UT	yes	broadband electrostatic waves ($f \leq f_{ce}$)
20.07.03. 06:19 – 11:00 UT	yes	broadband electrostatic waves ($f \leq f_{ce}$)
24.07.03. 21:27 – 22:40 UT	yes	broadband electrostatic waves ($f \leq f_{ce}$)
24.07.03. 23:03 – 24:00 UT	yes	broadband EME ($f \leq f_{ce}$), whistler waves
25.07.03. 06:59 – 08:39 UT	yes	broadband EME ($f \leq f_{ce}$), whistler waves, electron cyclotron waves
27.07.03. 13:45 – 15:24 UT	yes	broadband electrostatic waves ($f \leq f_{ce}$), electron cyclotron waves
29.07.03. 14:55 – 15:11 UT	yes	broadband electrostatic waves ($f \leq f_{ce}$)
29.07.03. 18:33 – 21:31 UT	yes	broadband electrostatic waves ($f \leq f_{ce}$), electron cyclotron waves
01.08.03. 00:20 – 02:06 UT	yes	broadband electrostatic waves ($f \leq f_{ce}$), electron cyclotron waves
01.08.03. 03:37 – 05:06 UT	yes	broadband electrostatic waves ($f \leq f_{ce}$)
01.08.03. 05:55 – 09:00 UT	yes	broadband EME ($f \leq f_{ce}$), whistler waves, electron cyclotron waves
05.08.03. 19:12 – 19:27 UT	yes	broadband electrostatic waves ($f \leq f_{ce}$)
08.08.03. 10:20 – 11:30 UT	yes	broadband EME ($f \leq f_{ce}$), whistler waves
12.08.03. 21:30 – 23:10 UT	no	broadband electrostatic waves ($f \leq f_{ce}$)
27.08.03. 07:23 – 08:40 UT	yes	broadband electrostatic waves ($f \leq f_{ce}$), electron cyclotron waves
05.09.03. 15:21 – 16:30 UT	yes	broadband EME ($f \leq f_{ce}$), whistler waves, electron cyclotron waves
15.09.03. 04:27 – 07:50 UT	yes	broadband electrostatic waves ($f \leq f_{ce}$)

24.09.03. 16:05 – 17:00 UT	yes	broadband electrostatic waves ($f \leq f_{ce}$)
29.09.03. 10:22 – 11:25 UT	yes	broadband EME ($f \leq f_{ce}$), whistler waves
01.10.03. 15:29 – 15:32 UT	yes	broadband electrostatic waves ($f \leq f_{ce}$)
08.10.03. 21:38 – 22:57 UT	yes	broadband EME ($f \leq f_{ce}$), whistler waves
11.10.03. 07:45-09:22 UT	yes	broadband electrostatic waves ($f \leq f_{ce}$), electron cyclotron waves
13.10.03. 11:40 – 13:10 UT	yes	broadband EME ($f \leq f_{ce}$), whistler waves
20.10.03. 15:35 – 18:10 UT	yes	broadband electrostatic waves ($f \leq f_{ce}$), electron cyclotron waves
03.08.04. 04:10 – 04:36 UT	yes	no evident wave activity
14.08.04. 22:00 – 23:00 UT	yes	broadband EME ($f \leq f_{ce}$), whistler waves
03.10.04. 16:43 – 17:55 UT	yes	broadband electrostatic waves ($f \leq f_{ce}$), electron cyclotron waves
03.10.04. 18:57 – 20:08 UT	yes	broadband EME ($f \leq f_{ce}$), whistler waves, electron cyclotron waves
06.10.04. 05:04 – 06:05 UT	yes	broadband EME ($f \leq f_{ce}$), whistler waves
08.10.04. 16:09 – 16:32 UT	yes	broadband EME ($f \leq f_{ce}$), whistler waves
11.10.04. 01:21:30–01:32 UT	yes	broadband electrostatic waves ($f \leq f_{ce}$)
11.10.04. 01:39 – 02:20 UT	yes	broadband electrostatic waves ($f \leq f_{ce}$), electron cyclotron waves
13.10.04. 07:02 -07:41 UT	yes	broadband EME ($f \leq f_{ce}$), whistler waves, electron cyclotron waves
15.10.04 13:54 – 14:36 UT	yes	broadband electrostatic waves ($f \leq f_{ce}$), electron cyclotron waves
22.10.04. 17:10 – 17:34 UT	yes	broadband EME ($f \leq f_{ce}$), whistler waves, electron cyclotron waves
22.10.04. 17:35 – 18:10 UT	yes	broadband EME ($f \leq f_{ce}$), whistler waves, electron cyclotron waves
22.10.04. 18:12 – 18:33 UT	yes	broadband electrostatic waves ($f \leq f_{ce}$), electron cyclotron waves
22.10.04. 18:44 – 19:05 UT	yes	electron cyclotron waves
22.10.04. 19:28 -19:31 UT	yes	broadband EME ($f \leq f_{ce}$), whistler waves, electron cyclotron waves
22.10.04. 19:32 – 20:35 UT	yes	electron cyclotron waves
07.08.05. 14:56 – 17:04 UT	yes	broadband EME ($f \leq f_{ce}$), whistler waves, electron cyclotron waves
09.08.05. 18:32 – 19:32 UT	yes	broadband electrostatic waves ($f \leq f_{ce}$), electron cyclotron waves
17.08.05. 00:38 – 02:16 UT	yes	broadband electrostatic waves ($f \leq f_{ce}$), electron cyclotron waves
21.08.05. 19:24 – 20:12 UT	yes	no evident wave activity
21.09.05. 14:13 – 14:19 UT	yes	broadband electrostatic waves and broadband EME ($f \leq f_{ce}$), whistler waves

21.09.05. 14:21 – 15:35 UT	yes	broadband EME ($f \leq f_{ce}$), whistler waves, electron cyclotron waves
28.09.05. 17:31 – 20:44 UT	yes	electron cyclotron waves
01.10.05. 04:44 – 04:50 UT	yes	broadband electrostatic waves ($f \leq f_{ce}$), electron cyclotron waves
01.10.05. 04:56 – 05:35 UT	yes	broadband EME ($f \leq f_{ce}$), whistler waves, electron cyclotron waves
15.10.05. 07:06 – 07:53 UT	yes	broadband electrostatic waves ($f \leq f_{ce}$)
17.10.05. 16:07 – 18:30 UT	yes	electron cyclotron waves

Acknowledgments

We acknowledge Cluster Science Archive (http://www.cosmos.esa.int/web/csa), PI and teams of CIS, PEACE, FGM and STAFF instruments for providing the data. The Cluster data used in this study were downloaded from the Cluster Science Archive version 1.2.1 at http://www.cosmos.esa.int/web/csa. To obtain the data, one should start the CSA GRAPHICAL USER INTERFACE; and then to download the data, just select the particular instrument and time interval.

The work of E.E. Grigorenko, E. A. Kronberg and P. W. Daly was supported by the Volskwagen Foundation (grant Az 90 312). P. W. Daly and E. A. Kronberg acknowledge the Deutsches Zentrum für Luft and Raumfahrt (DLR) for supporting the RAPID instrument at MPS under grant 50 OC 1401. N.Yu. Ganushkina and E.E. Grigorenko are thankful for the support received from the Academy of Finland as Space Cooperation in the Science and Technology Commission between Finland and Russia (TT/AVA). N.Yu. Ganushkina acknowledges that the part of the research leading to these results has received funding from the European Union Seventh Framework Programme (FP7/2007-2013) under grant agreements 606716 SPACESTORM and from the European Union's Horizon 2020 research and innovation programme under grant agreement 637302 PROGRESS. E.A. Kronberg and N.Yu. Ganushkina thanks the International Space Science

Institute in Bern, Switzerland, for their support of the international teams on “Analysis of Cluster Inner Magnetosphere Campaign data, in application the dynamics of waves and wave-particle interaction within the outer radiation belt” and “Ring current modeling: Uncommon Assumptions and Common Misconceptions”. The work of N.Yu. Ganushkina was also partly supported by NASA award NNX14AF34G. Work at IRAP was supported by CNRS and CNES. L.M. Zelenyi acknowledges the Russian Academy of Science (grant P-7) and Russian Foundation for Basic Research (project Nr.16-52-16009) for the support of his work.

References

Angelopoulos, V., W. Baumjohann, C.F. Kennel, F.V. Coroniti, M.G. Kivelson, R. Pellat, R.J. Walker, H. Lühr, G. Paschmann (1992), Bursty bulk flows in the inner central plasma sheet, J. Geophys. Res., 97, 4027-4039.

Artemyev, A. V., W. Baumjohann, A. A. Petrukovich, R. Nakamura, I. Dandouras, and A. Fazakerley (2011), Proton/electron temperature ratio in the magnetotail, Ann. Geophys., 29, 2253–2257, doi:10.5194/angeo-29-2253-2011.

Ashour-Abdalla, M., Berchem, J. P., Buechner, J., and Zelenyi, L. M. (1993), Shaping of the magnetotail from the mantle – Global and local structuring, J. Geophys. Res., 98, 5651–5676, doi:10.1029/92JA01662.

Ashour-Abdalla, M., Frank, L. A., Paterson, W. R., Peroomian, V., and Zelenyi, L. M. (1996), Proton velocity distributions in the magnetotail: Theory and observations, J. Geophys. Res., 101, 2587– 2598, doi:10.1029/95JA02539.

Balogh, A., et al. (2001), The Cluster magnetic field investigation: Overview of in-flight performance and initial results, Ann. Geophys., 19, 1207–1217.

Baumjohann, W., Paschmann, G., and Cattell, C. A. (1989), Average plasma properties in the central plasma sheet, J. Geophys. Res., 94, 6597–6606, doi:10.1029/JA094iA06p06597.

J. Birn, M. Hesse, R. Nakamura, S. Zaharia (2013) Particle acceelration in dipolarization events, J. Geophys. Res., 118, 1960-1971, doi:10.1002/jgra.50132.

J. Birn, A. Runov and M. Hesse (2014), Energetic electrons in dipolarization events: Spatial properties and anisotropy, J. Geophys. Res., 119, 3604-3616, doi: 10.1002/2013JA019738.

Biskamp D. (2000), *Magnetic Reconnection in Plasmas*, Cambridge Univ. Press, New York.

Cornilleau-Wehrlin N. et al. (2003), First results obtained by the Cluster STAFF experiment, Ann. Geophys., 21, 437-456.

Daly, P. W., and E. A. Kronberg (2015), User guide to the RAPID measurements in the Cluster Active Archive (CAA), Tech. Rep. CAA–EST–UG–RAP, European Space Agency, Paris.

Deng X., M. Ashour-Abdalla, M. Zhou, R. Walker, M. El-Alaoui, V. Angelopoulos, R.E. Ergun, D. Schriver (2010), Wave and particle characteristics of earthward injections associated with dipolarization fronts, J. Geophys. Res., 115, A09225, doi:10.1029/2009JA015107.

Drake J.F., M. Swisdak, H. Che, M.A. Shay (2006), Electron acceleration from contracting magnetic islands during reconnection, Nature 443, 553–556, doi:10.1038/nature05116.

Farrell W.M., M.D. Desch, K.W. Ogilvie, M.L. Kaiser, and K. Goetz (2003), The role of upper hybrid waves in magnetic reconnection, Geophys. Res. Lett., 30(24),2259, doi:10.1029/2003GL017549.

Fu, H. S., Y. V. Khotyaintsev, M. André, and A. Vaivads (2011), Fermi and betatron acceleration of suprathermal electrons behind dipolarization fronts, Geophys. Res. Lett., 38, L16104, doi:10.1029/2011GL048528.

Fu, H. S., Y. V. Khotyaintsev, A. Vaivads, M. André, V. A. Sergeev, S. Y. Huang, E. A. Kronberg, and P. W. Daly (2012a), Pitch angle distribution of suprathermal electrons behind dipolarization fronts: A statistical overview, J. Geophys. Res., 117, A12221, doi:10.1029/2012JA018141.

Fu, H. S., Y. V. Khotyaintsev, A. Vaivads, M. André, and S. Y. Huang (2012b), Occurrence rate of earthward-propagating dipolarization fronts, Geophys. Res. Lett., 39, L10101, doi:10.1029/2012GL051784.

Fu, H. S., Y. V. Khotyaintsev, A. Vaivads, A. Retino, and M. Andre (2013a), Energetic electron acceleration by unsteady magnetic reconnection, Nature Physics, 9, 426-430, doi:10.1038/nphys2664.

Fu, H. S., et al. (2013b), Dipolarization fronts as a consequence of transient reconnection: In situ evidence, Geophys. Res. Lett., 40, 6023-6027, doi:10.1002/2013GL058620.

Fu, H. S., et al. (2014), Whistler-mode waves inside flux pileup region: Structured or unstructured?, J. Geophys. Res. Space Physics, 119, 9089-9100, doi:10.1002/2014JA020204

Gurnett, D. A., Frank, L. A., Lepping, R. P., et al.: Plasma waves in the distant magnetotail, J. Geophys. Res., 81, 6059–6071, 1976.

Hoshino M. (2005), Electron surfing acceleration in magnetic reconnection. J. Geophys. Res. 110 (A9), A10215 , doi:10.1029/2005JA011229.

Hoshino M., T. Mukai, T. Yamamoto, S. Kokubun (1998), Ion dynamics in magnetic reconnection: Comparison between numerical simulation and Geotail observations, *J. Geophys. Res.*, *103*, A3, 4509-4530.

Hoshino, M., K. Hiraide, and T. Mukai (2001), Strong electron heating and non-Maxwellian behavior in magnetic reconnection, Earth Planets Space, 53, 627– 634.

Hwang K.-J., M.L. Goldstein, E. Lee, J.S. Pickett (2011), Cluster observations of multiple dipolarization fronts, J. Geophys. Res., 116, A00132, doi:10.1029/2010JA015742.

Johnstone, A.D., et al. (1997), PEACE: A plasma electron and current experiment, Space Sci. Rev., 79, 351-398.

Imada S., R. Nakamura, P. W. Daly, M. Hoshino, W. Baumjohann, S. Mühlbachler, A. Balogh, and H. Réme, Energetic electron acceleration in the downstream reconnection outflow region, J. Geophys. Res., 112, A03202, doi:10.1029/2006JA011847, 2007

Kaufmann, R. L., Paterson, W. R., and Frank, L. A. (2005), Relationships between the ion flow speed, magnetic flux transport rate, and other plasma sheet parameters, J. Geophys. Res., 110, A09216, doi:10.1029/2005JA011068.

Khotyaintsev Yu.V., C. M. Cully, A. Vaivads, and M. André (2011), Plasma Jet Braking: Energy Dissipation and Nonadiabatic Electrons, PRL, 106, DOI: 10.1103/PhysRevLett.106.165001.

Kronberg E. A., E.E. Grigorenko, S. E. Haaland, P. W. Daly, D. C. Delcourt, H. Luo, L. M. Kistler and I. Dandouras (2015), Distribution of energetic oxygen and hydrogen in the near-Earth plasma sheet, J. Geophys. Res., Vol. 120, 10.1029/2014JA020882.

Lavraud B., J. E. Borovsky, V. Génot, S. J. Schwartz, J. Birn, A. N. Fazakerley, M. W. Dunlop, M. G. G. T. Taylor, H. Hasegawa, A. P. Rouillard, J. Berchem, Y. Bogdanova, D. Constantinescu, I. Dandouras, J. P. Eastwood, C. P. Escoubet, H. Frey, C. Jacquey, E. Panov, Z. Y. Pu, C. Shen, J. Shi, D. G. Sibeck, M. Volwerk, and J. A. Wild (2009), Tracing solar wind plasma entry into the magnetosphere using ion-to-electron temperature ratio, Gephys. Res. Lett., 36, L18109, doi:10.1029/2009GL039442

Le Contel O., et al. (2009), Quasi-parallel whistler mode waves observed by THEMIS during near-Earth dipoalrizations, Ann. Geophys., 27, 2259 – 2275.

Lui A.T.Y. (2004), Potential plasma instabilities for substorm expansion onsets, Space Science Reviews, 113, 127–206.

Lui A.T.Y., P.H. Yoon, C. Mok and C.-M. Ryu (2008), Inverse cascade feature in current disruption, J. Geophys. Res., 113, A00C06, doi:10.1029/2008JA013521.

Lyons, L. R. (1984), Electron energization in the geomagnetic tail current sheet, J. Geophys. Res., 89, 5479–5487, doi:10.1029/JA089iA07p05479.

Matsumoto H., H. Kojima, Y. Kasaba, T. Miyake, Y. Omura, M. Okada, I. Nagano, M. Tsutsui (1994), Electrostatic solitary waves (ESW) in the magnetotail: BEN wave forms observed by GEOTAIL, Geophys. Res. Lett., 21, 2015.

Nakamura R., et al. (2002), Motion of the dipolarization front during a flow burst event observed by Cluster, Geophys. Res. Lett., 29(20), 1942, doi:10.1029/2002GL015763.

R. Nakamura, A Retinò, W. Baumjohann, M. Volwerk, N. Erkaev, B. Klecker, E.A. Lucek, I. Dandouras, M. André, Y. Khotyaintsev (2009), Evolution of dipolarization in the near_earth current sheet indiced by Earthward rapid flux transport, Ann. Geophys., 27, 1743-1754.

Ohtani S.I., M.A. Shay, T. Mukai (2004), Temporal structure of the fast convective flow in the plasma sheet: Comparison between observations and two-fluid simulations, J. Geophys. Res., 109, A03210, doi:10.1029/2003JA10002.

Oka M., T.D. Phan, S. Krucker,M. Fujimoto, I. Shinohara, Electron acceleration by multi-island coalescence (2010), Astrophys. J., 714, 915–926, doi:10.1088/0004-637X/714/1/915.

Petkaki P., M.P. Freeman, A.P. Walsh (2006), Cluster observations of broadband electromagnetic waves in and around a reconnection region in the Earth's magnetotail current sheet, Geophys. Res. Lett., 33, L10105, doi:10.1029/2006GL027066.

Réme, H., C. Aoustin, J. M. Bosqued, I. Dandouras et al. (2001), First multispacecraft ion measurements in and near the Earth's magnetosphere with identical Cluster ion spectrometry (CIS) experiment, Ann. Geophys., 19, 1303.

Runov A., V. Angelopoulos, M.I. Sitnov, V.A. Sergeev, J. Bonnell, J.P. McFadden, D. Larson, K. Glassmeier, U. Auster (2009), THEMIS observations of an earthward-propagating dipolarization front. Geophys. Res. Lett. 36, L14106, doi:10.1029/2009GL038980.

Runov A., V. Angelopoulos, C. Gabrielse, J. Liu. D.L. Turner, X.-Z. Zhou (2015), Average thermodynamic and spectral properties of plasma in and around dipolarizing flux bundles, J. Geophys. Res., 120, 4369-4383, doi:10.1002/2015JA021166.

Sergeev V.A., V. Angelopoulos, J.T. Gosling, C.A. Cattel, C.T. Russell (1996), Detection of localized plasma-depleted flux tubes or bubbles in the midtail plasma sheet, J. Geophys. Res., 101, 10,817-10,826.

Sergeev, V.A., V. Angelopoulos, and R. Nakamura (2012), Recent advances in understanding substorm dynamics, Geophys. Res. Lett., 39, L05101, doi:10.1029/2012GL050859.

V.A. Sergeev, N.P. Dmitrieva, N.A. Stepanov, D.A. Sormakov, V. Angelopoulos, A.V. Runov (2015), On the plasma sheet dependence on solar wind and substorms and its role in magnetosphere-ionosphere coupling, Earth, Planets and Space, 67:133, doi:10.1186/s40623-015-0296-x.

Sitnov M.I, M. Swisdak, A.V. Divin (2009), Dipolarization fronts as a signature of of transient reconnection in the magnetotail, J. Geophys. Res., 114, A04202, doi:10.1029/2008JA013980.

Sharma S., R. Nakamura, A. Runov, E. E. Grigorenko, H. Hasegawa, M. Hoshino, P. Louarn, C. J. Owen, A. Petrukovich, J.-A. Sauvaud, V. S. Semenov, V. A. Sergeev, J. A. Slavin, B. U. Ö.

Sonnerup, L. M. Zelenyi, G. Fruit, S. Haaland, H. Malova, and K. Snekvik (2008), Transient and Localized Processes in the Magnetotail: A Review, Annales Geophysicae, 26, 955–1006.

Shiokawa K., W. Baumjohann, G. Haerendel (1997), Braking of high-speed flows in the near-Earth tail, Geophys. Res. Lett., 24, 1179-1182, doi:10.1029/97GL01062.

Viberg H., Yu.V. Khotyaintsev, A. Vaivads, M. André, H.S. Fu, N. Cornilleau-Wehrlin (2104), Whistler mode waves at magnetotail dipolarization fronts, J. Geophys. Res., 119, 2605-2611, doi:10.1002/2014JA019892.

Wang C.-P., M. Gkioulidou, L.R. Lyons, V. Angelopoulos (2012), Spatial distributions of the ion to electron temperature ratio in the magnetosheath and plasma sheet, J. Geophys. Res., 117, A08215, doi:10.1029/2012JA017658.

Wilken, B., et al. (2001), First results from the RAPID imaging energetic particle spectrometer on board Cluster, Ann. Geophys., 19, 1355–1366.

Zelenyi L.M., D.V. Zogin, J. Buechner (1990), Quasiadiabatic dynamics of charged particles in the tail of the magnetosphere, Cosmic Res. (English edition), 28, 3, 369-381.

Zhang X., V. Angelopoulos (2014), On the relationship of electrostatic cyclotron harmonic emissions with electron injections and dipolarization fronts, J. Geophys. Res., 119, 2536-2549, doi:10.1002/2013JA019540.

Zhou M., M. Ashour-Abdalla, X. Deng, D. Schriver, M. El-Alaoui, Y. Pang (2009), THEMIS observation of multiple dipolarization fronts and associated wave characteristics in the near-Earth magnetotail, Geophys. Res. Lett., 36, L20107,doi:10.1029/2009GL040663.

Figure Captions

Figure 1. The scatterplots of the PS samples using in our studies in the (*YZ*) and (*XY*) planes.

Figure 2. From top to bottom: (a): the statistical distribution of the average values of $<T_p/T_e>$ in the (*XY*) plane. The $<T_p/T_e>$ were averaged over $2R_E$ x $2R_E$ bin. The colored scale in the right part of the Figure displays the values of $<T_p/T_e>$. (b): the $<T_p/T_e>(R)$ profile integrated over all *Y* locations for a given *R*-bin. (c): the $<T_p/T_e>(Y)$ profile integrated over all *R* locations for a given *Y*-bin. (d): a histogram of the occurrence frequency distribution of the T_p/T_e observed in the PS samples from our data base.

Figure 3. An example of the PS crossing by Cl-1 On 8.10.2001, in which the decreases of T_p/T_e below 3.5 were observed. From top to bottom: the Energy-Time spectrograms of omni-directional electrons (PEACE data) (a) and protons (CODIF data) (b); the time profiles of the T_p (black line) and T_e (red line) (c); T_p/T_e (d); and T_{PAR}/T_{PER} fro protons (black line) and electrons (red line) (e); the three components of the magnetic field (f); the frequency spectra of the electric |E| (g) and magnetic |B| (h) field fluctuations in frequency range 8 - 4096 Hz; the time-frequency distribution of the value of angle between the Poynting flux of electromagnetic fluctuations and the ambient magnetic field (i) obtained by STAFF experiment. The time profiles of f_{ce}, f_{pp} and f_{LH} are shown by the white, magenta and black lines respectively in panels (g,h) and by the purple, magenta and black lines respectively in panel (i).

Figure 4. The zoom of the interval "II", in which the minimum of T_p/T_e was observed (see Figure 3). From top to bottom: time profiles of *X*-component of proton bulk velocity (a) of proton (in black) and of electron (in red) $T_{||}$ and $T_{\perp}$ (b); the variations of electron temperature ΔT_e observed by PEACE instrument (in red) and the variations of electron temperature expected from the betatron heating $\Delta T_{e\_betatron}$ (in black) (c); the time profile of the magnetic fluctuations power δB^2 integrated in $[f_{pp},f_{ce}]$ frequency range (d); the time profile of T_p/T_e (e); three components of the magnetic field (f) and STAFF observations in the same format as in Figure 3 (g-i).

Figure 5. Pitch angle distributions (PAD) of electrons and the spectra of electric |*E*| and magnetic |*B*| field fluctuations observed in three time periods ("1-3") marked by the blue horizontal lines in Figure 4.

Figure 6. The results of epoch superposition analysis applied to the intervals listed in Tab.1 (see the Appendix). From top to bottom: the epoch profiles of $AE(t)$; $\beta(t)$; $V_X(t)$; $T_p(t)$; $T_e(t)$; $[T_p/T_e](t)$ and the B_Z^* (t) and the power of electric and magnetic field fluctuations integrated with the frequency range $[f_{pp}, f_{ce}]$. The red dashed line indicates the onset of dipolarization in each event from our data base. The horizontal blue line shows the "turbulent" phase of dipolarizations. The scatterplots of low and upper quartiles of the corresponding data sets used for the epoch analysis are displayed by the grey dots.

Figure 7 A scatterplot of variation ΔT_e versus ΔT_p at the moments of minimum T_p/T_e observation in the PS intervals listed in Tab.1.

Figure 8. Left column: scatterplots of T_e versus the power of electric and magnetic field fluctuations integrated with the frequency range [f_{pp}, f_{ce}] observed during the PS intervals listed in Tab.1. Right column: the same for T_p/T_e.

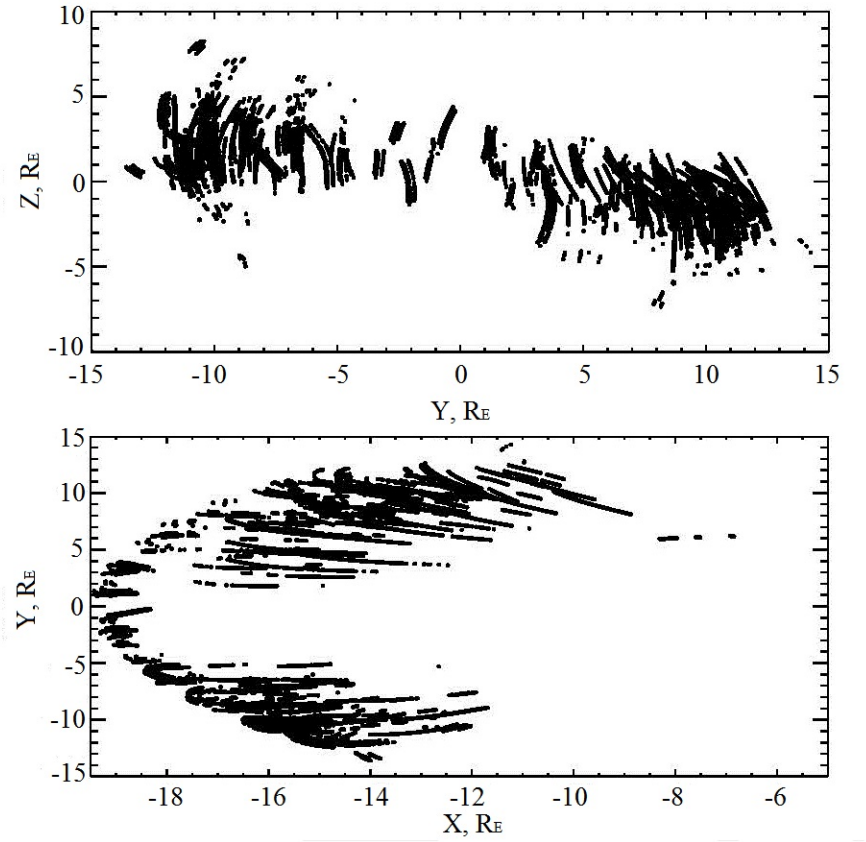

Figure 1. The scatterplots of the PS samples using in our studies in the (*YZ*) and (*XY*) planes.

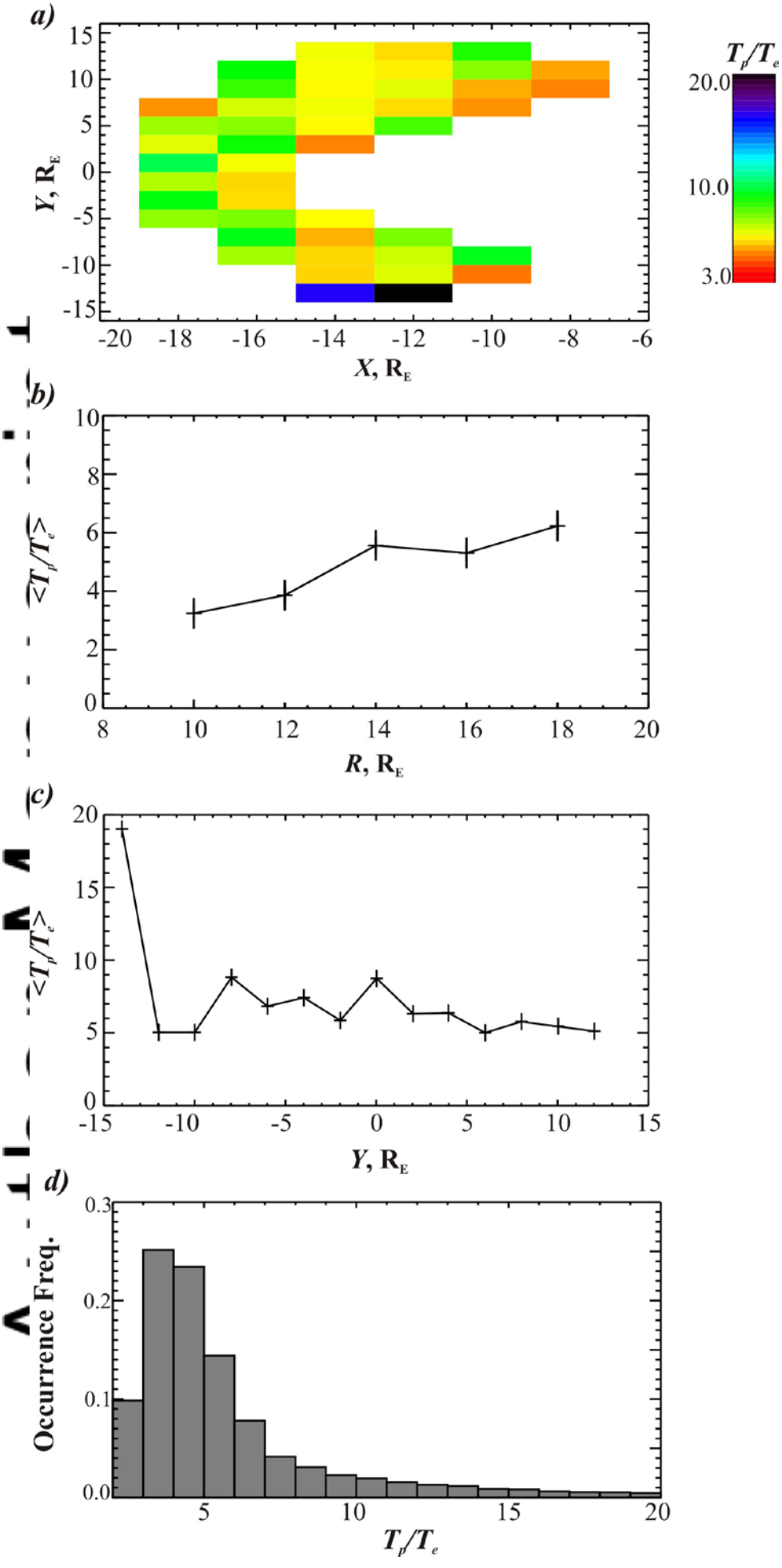

Figure 2. From top to bottom: (a): the statistical distribution of the average values of $<T_p/T_e>$ in the (*XY*) plane. The $<T_p/T_e>$ were averaged over $2R_E$ x $2R_E$ bin. The colored scale in the right part of the Figure displays the values of $<T_p/T_e>$. (b): the $<T_p/T_e>(R)$ profile integrated over all *Y* locations for a given *R*-bin. (c): the $<T_p/T_e>(Y)$ profile integrated over all *R* locations for a given *Y*-bin. (d): a histogram of the occurrence frequency distribution of the T_p/T_e observed in the PS samples from our data base.

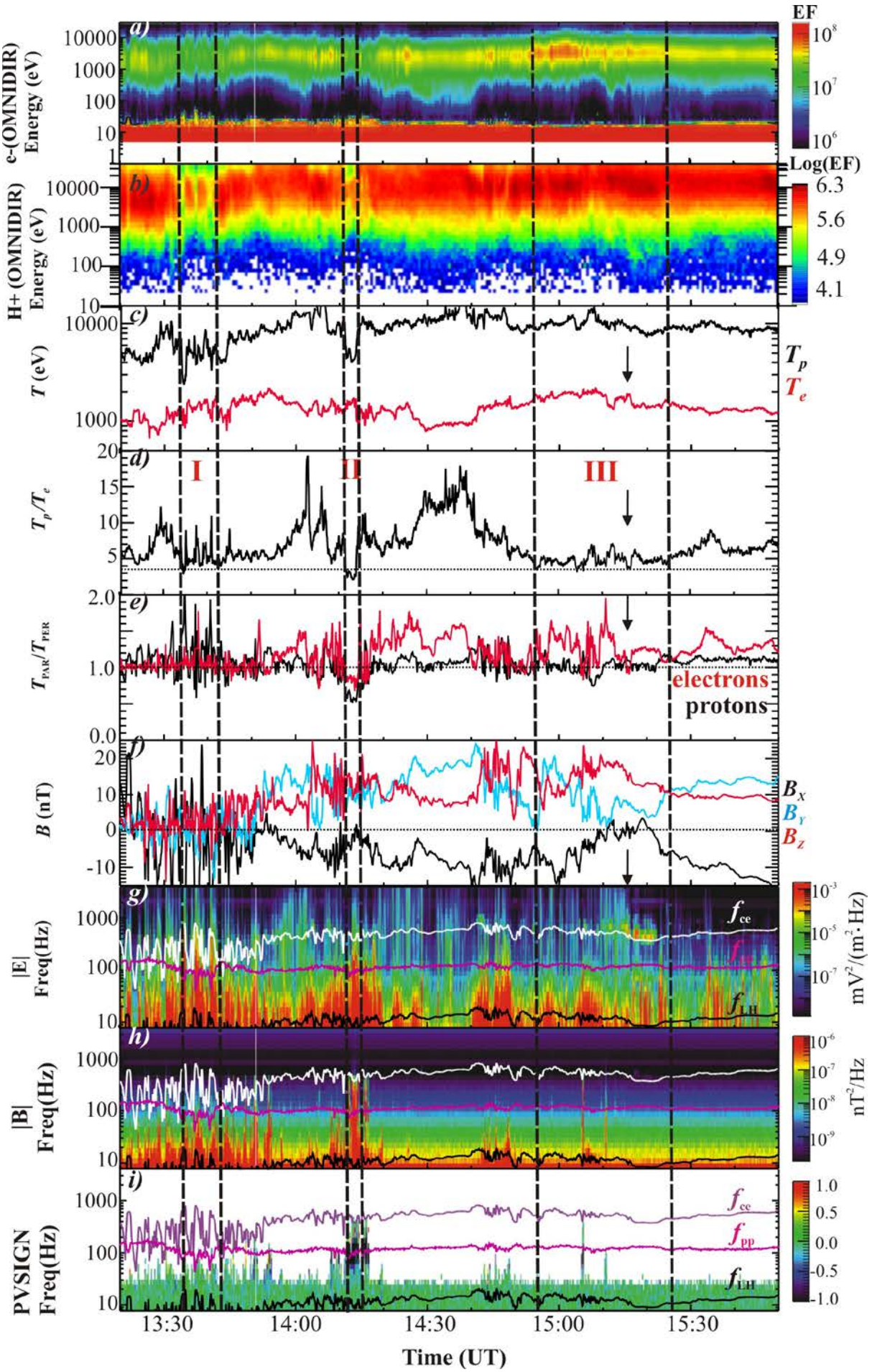

Figure 3. An example of the PS crossing by Cl-1 On 8.10.2001, in which the decreases of T_p/T_e below 3.5 were observed. From top to bottom: the Energy-Time spectrograms of omni-directional electrons (PEACE data) (a) and protons (CODIF data) (b); the time profiles of the T_p (black line) and T_e (red line) (c); T_p/T_e (d); and T_{PAR}/T_{PER} fro protons (black line) and electrons (red line) (e); the three components of the magnetic field (f); the frequency spectra of the electric |E| (g) and magnetic |B| (h) field fluctuations in frequency range 8 - 4096 Hz; the time-frequency distribution of the value of angle between the Poynting flux of electromagnetic fluctuations and the ambient magnetic field (i) obtained by STAFF experiment. The time profiles of f_{ce}, f_{pp} and f_{LH} are shown by the white, magenta and black lines respectively in panels (g,h) and by the purple, magenta and black lines respectively in panel (i).

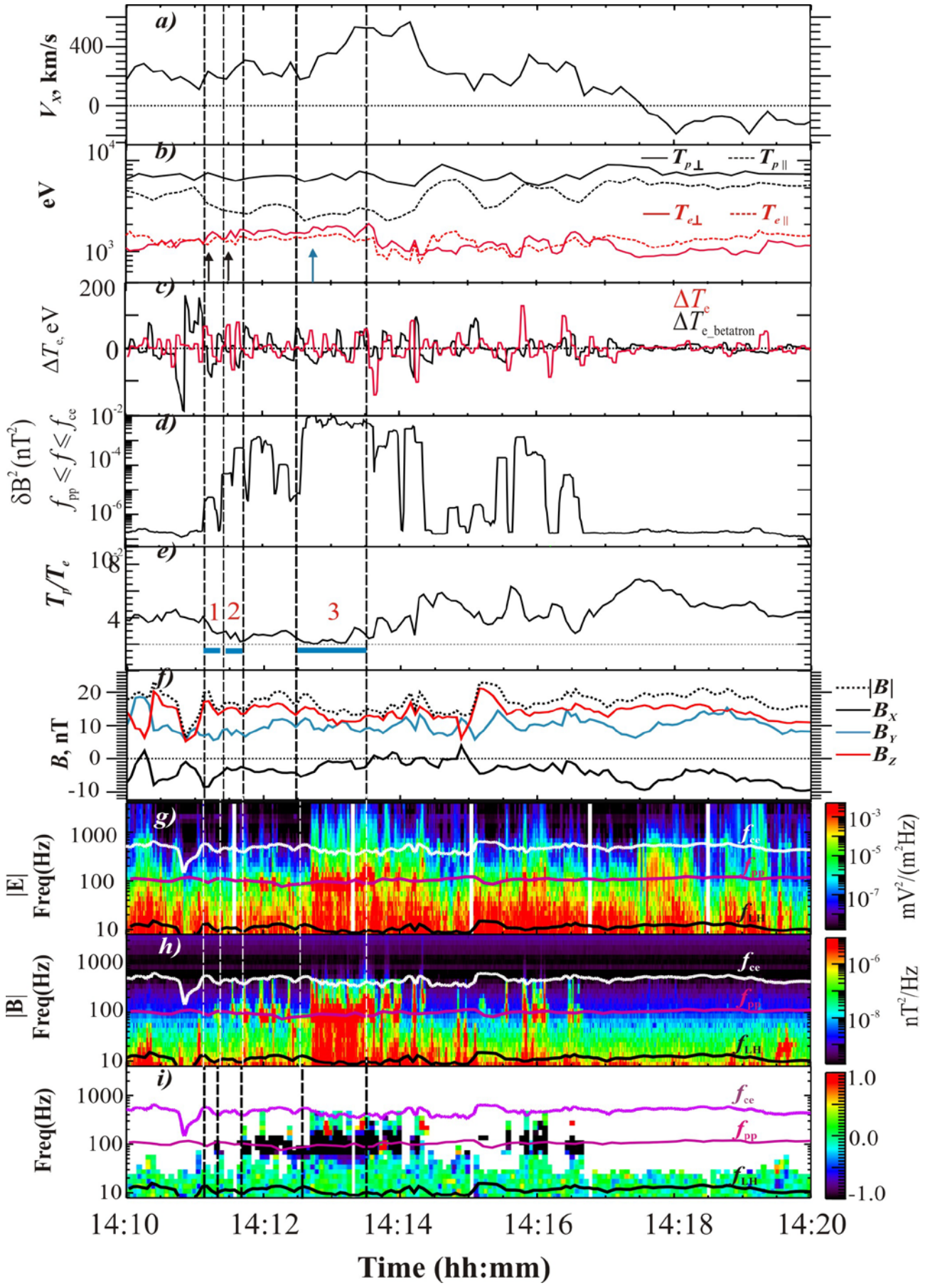

Figure 4. The zoom of the interval "II", in which the minimum of T_p/T_e was observed (see Figure 3). From top to bottom: time profiles of *X*-component of proton bulk velocity (a) of proton (in black) and of electron (in red) $T_{||}$ and $T_{\perp}$ (b); the variations of electron temperature ΔT_e observed by PEACE instrument (in red) and the variations of electron temperature expected from the betatron heating $\Delta T_{e\_betatron}$ (in black) (c); the time profile of the magnetic fluctuations power δB^2 integrated in $[f_{pp},f_{ce}]$ frequency range (d); the time profile of T_p/T_e (e); three components of the magnetic field (f) and STAFF observations in the same format as in Figure 3 (g-i).

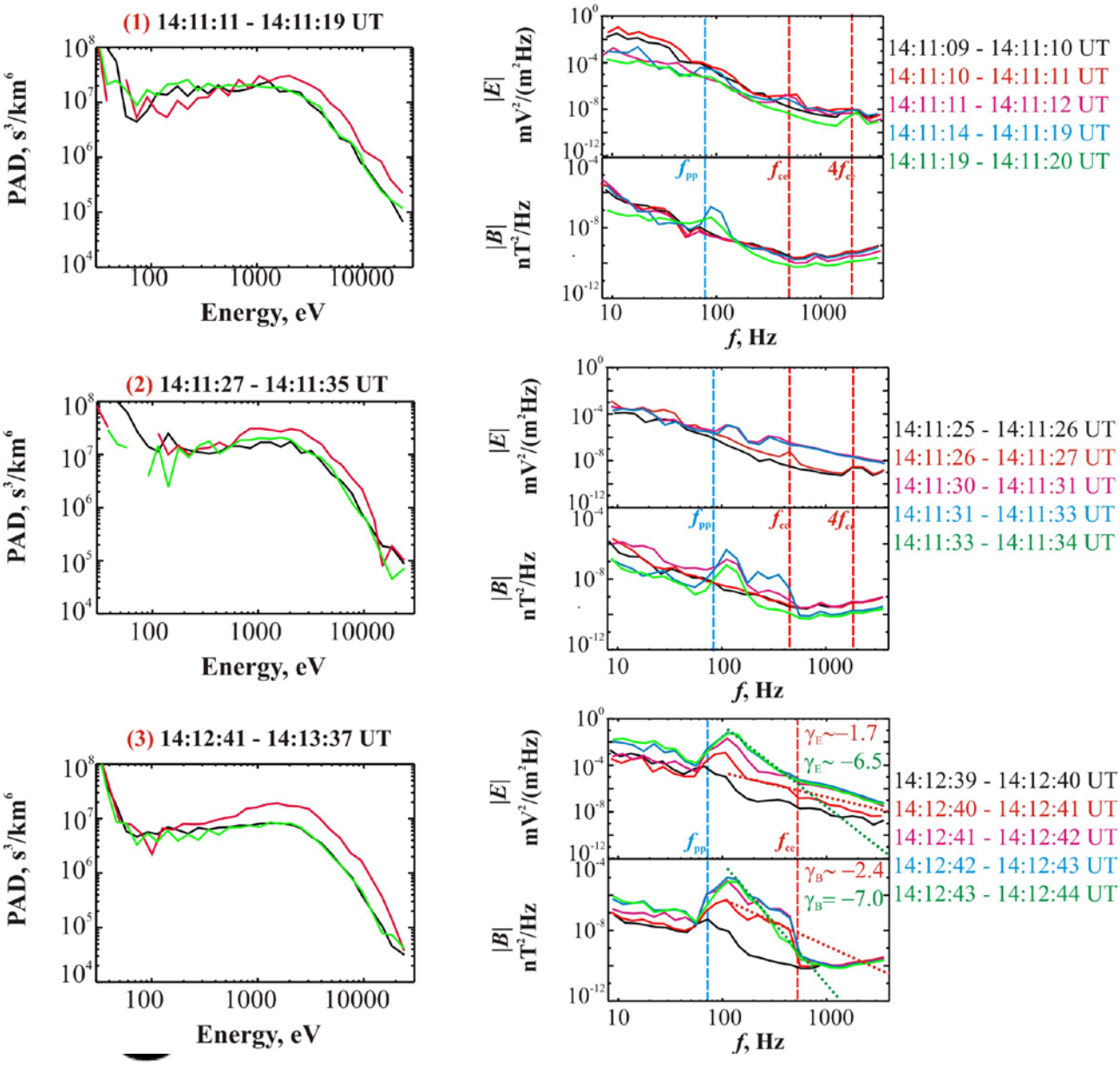

Figure 5. Pitch angle distributions (PAD) of electrons and the spectra of electric |*E*| and magnetic |*B*| field fluctuations observed in three time periods ("1-3") marked by the blue horizontal lines in Figure 4.

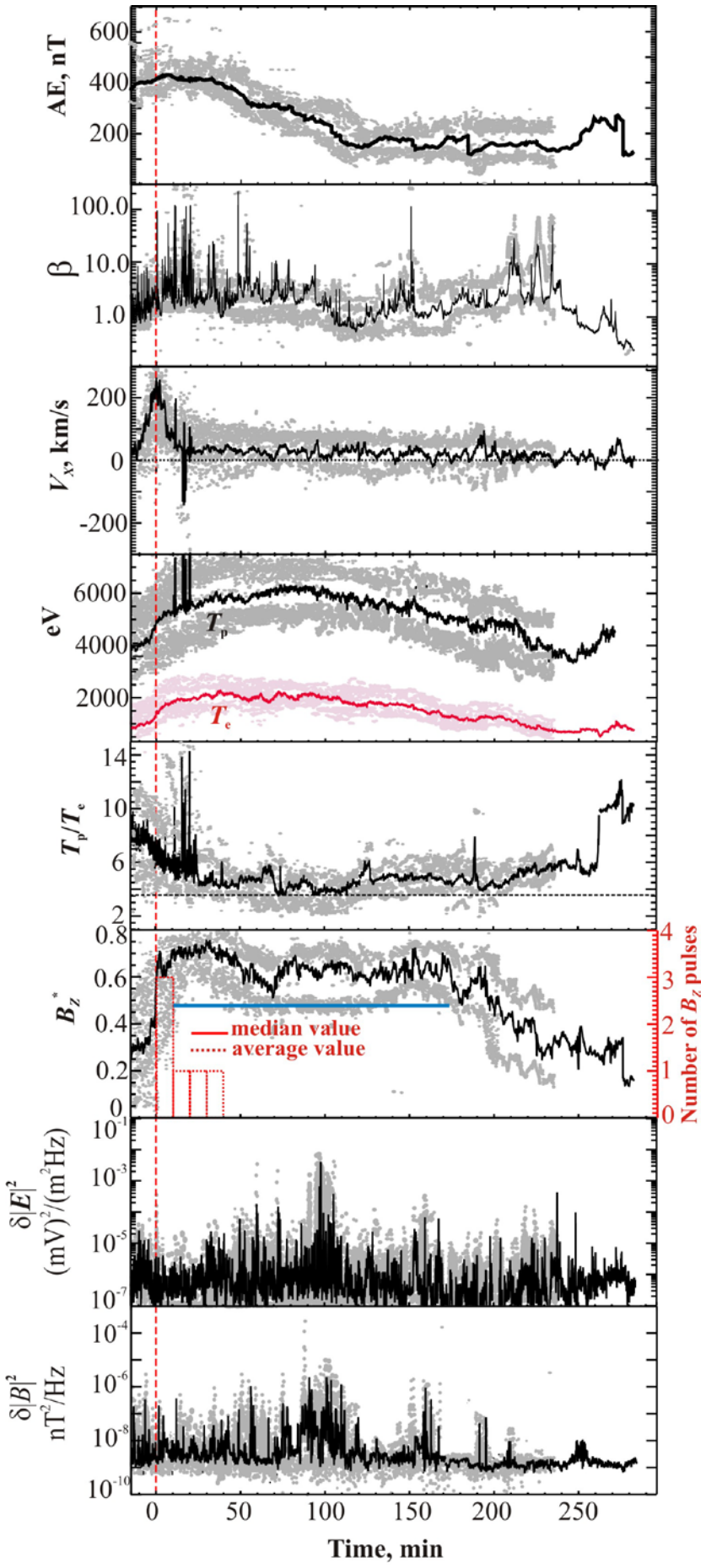

Figure 6. The results of epoch superposition analysis applied to the intervals listed in Tab.1 (see the Appendix). From top to bottom: the epoch profiles of $AE(t)$; $\beta(t)$; $V_X(t)$; $T_p(t)$; $T_e(t)$; $[T_p/T_e](t)$ and the B_Z^* (t) and the power of electric and magnetic field fluctuations integrated with the frequency range $[f_{pp}, f_{ce}]$. The red dashed line indicates the onset of dipolarization in each event from our data base. The horizontal blue line shows the "turbulent" phase of dipolarizations. The scatterplots of low and upper quartiles of the corresponding data sets used for the epoch analysis are displayed by the grey dots

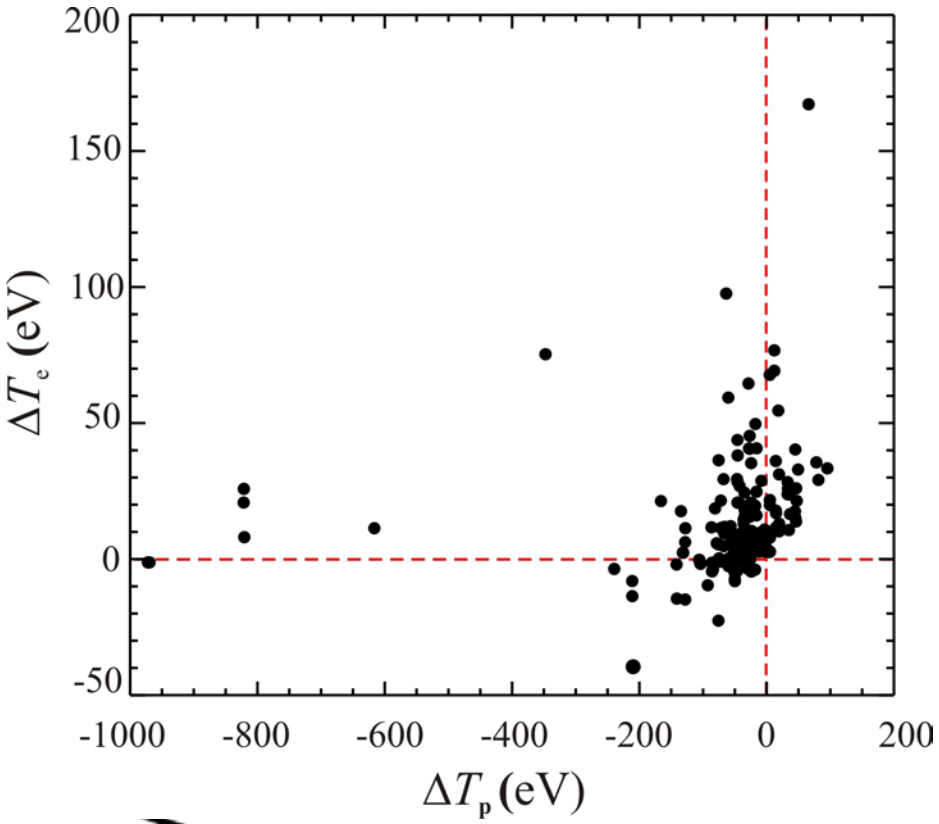

Figure 7 A scatterplot of variation ΔT_e versus ΔT_p at the moments of minimum T_p/T_e observation in the PS intervals listed in Tab.1.

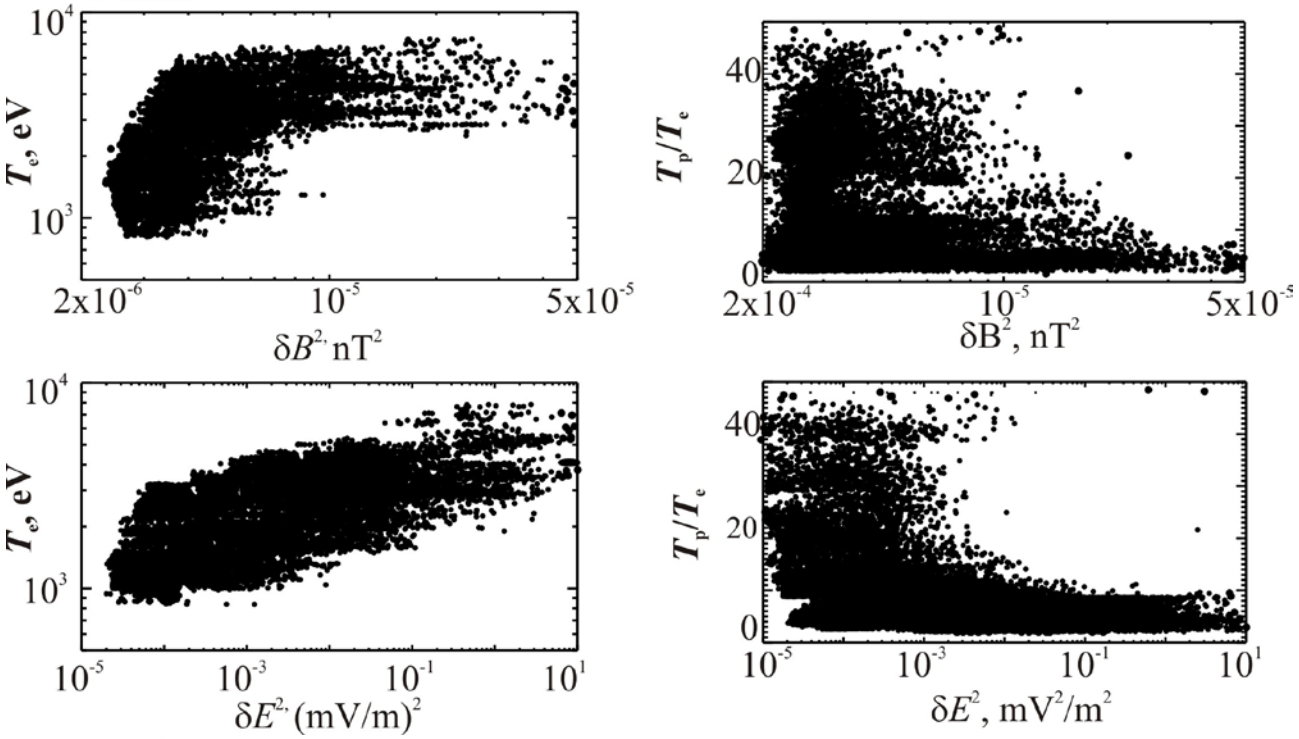

Figure 8. Left column: scatterplots of T_e versus the power of electric and magnetic field fluctuations integrated with the frequency range [f_{pp}, f_{ce}] observed during the PS intervals listed in Tab.1. Right column: the same for T_p/T_e.

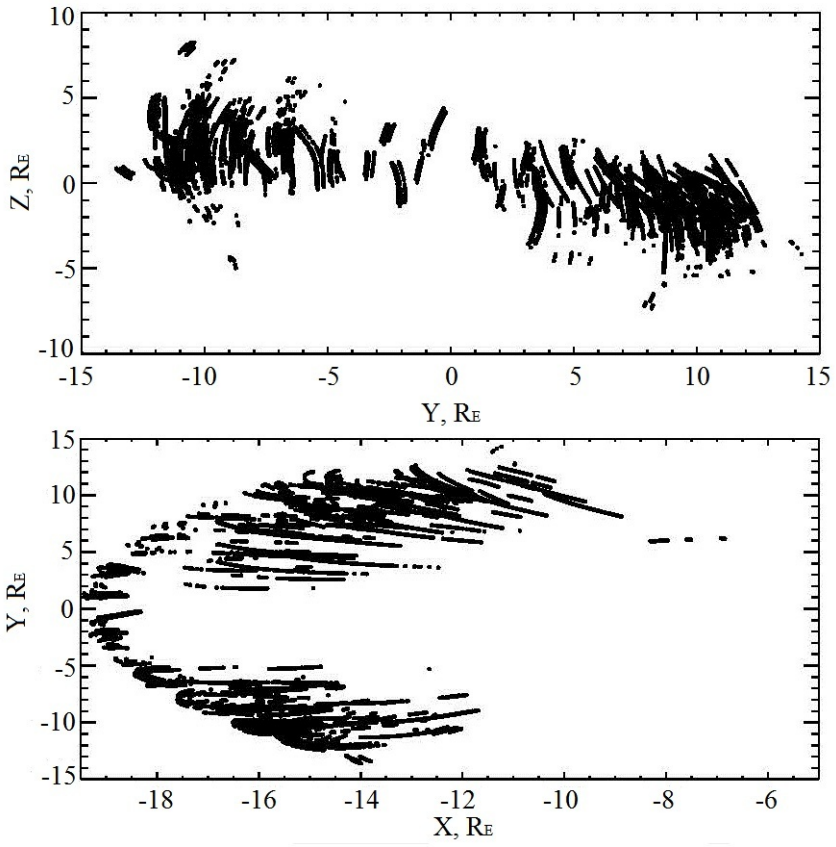

2016JA022874-f01-z-.jpg

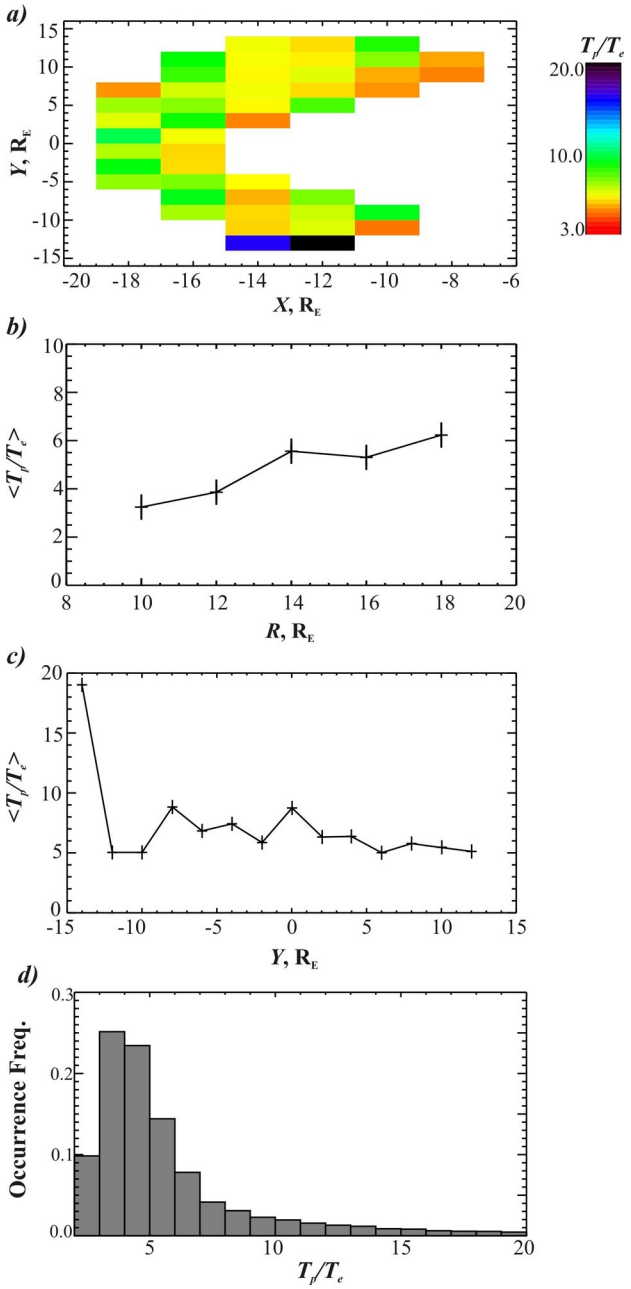

2016JA022874-f02-z-.jpg

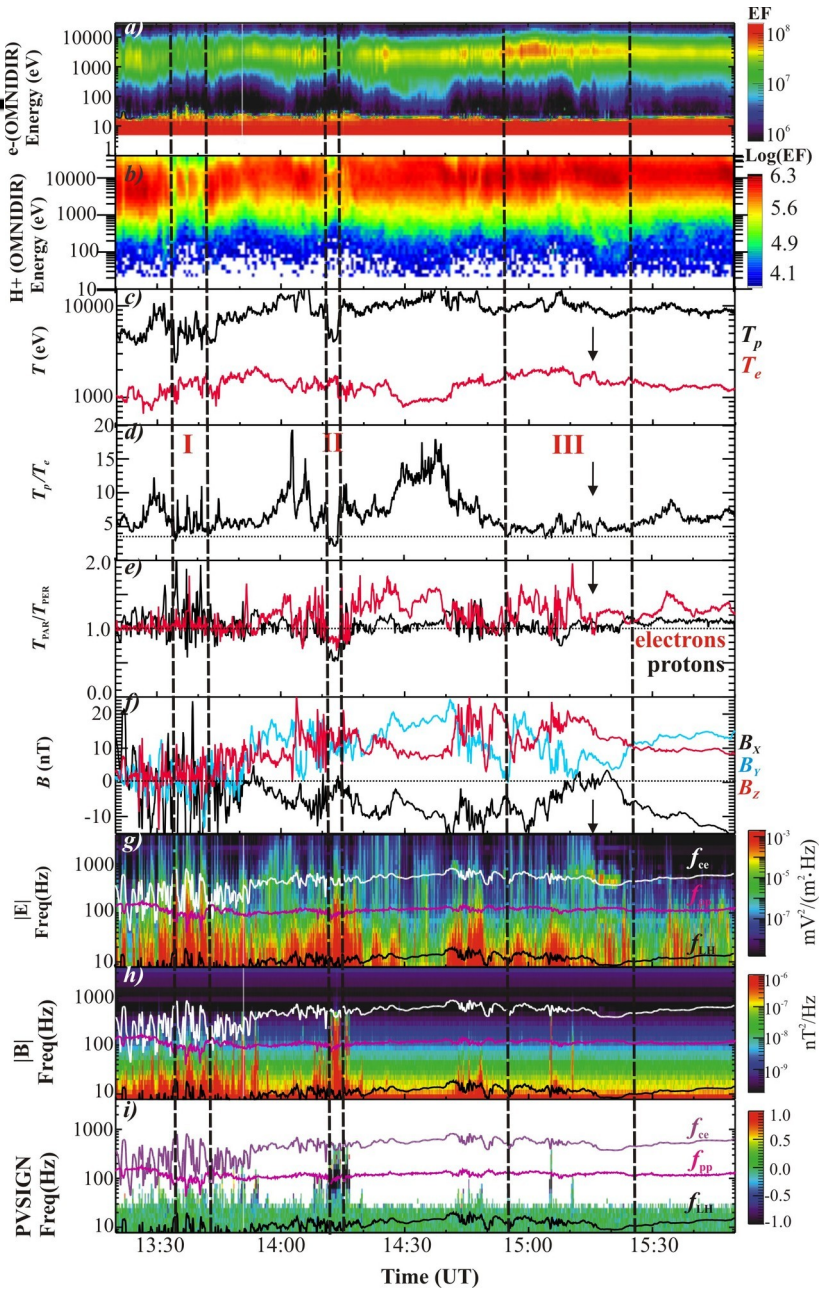

2016JA022874-f03-z-.jpg

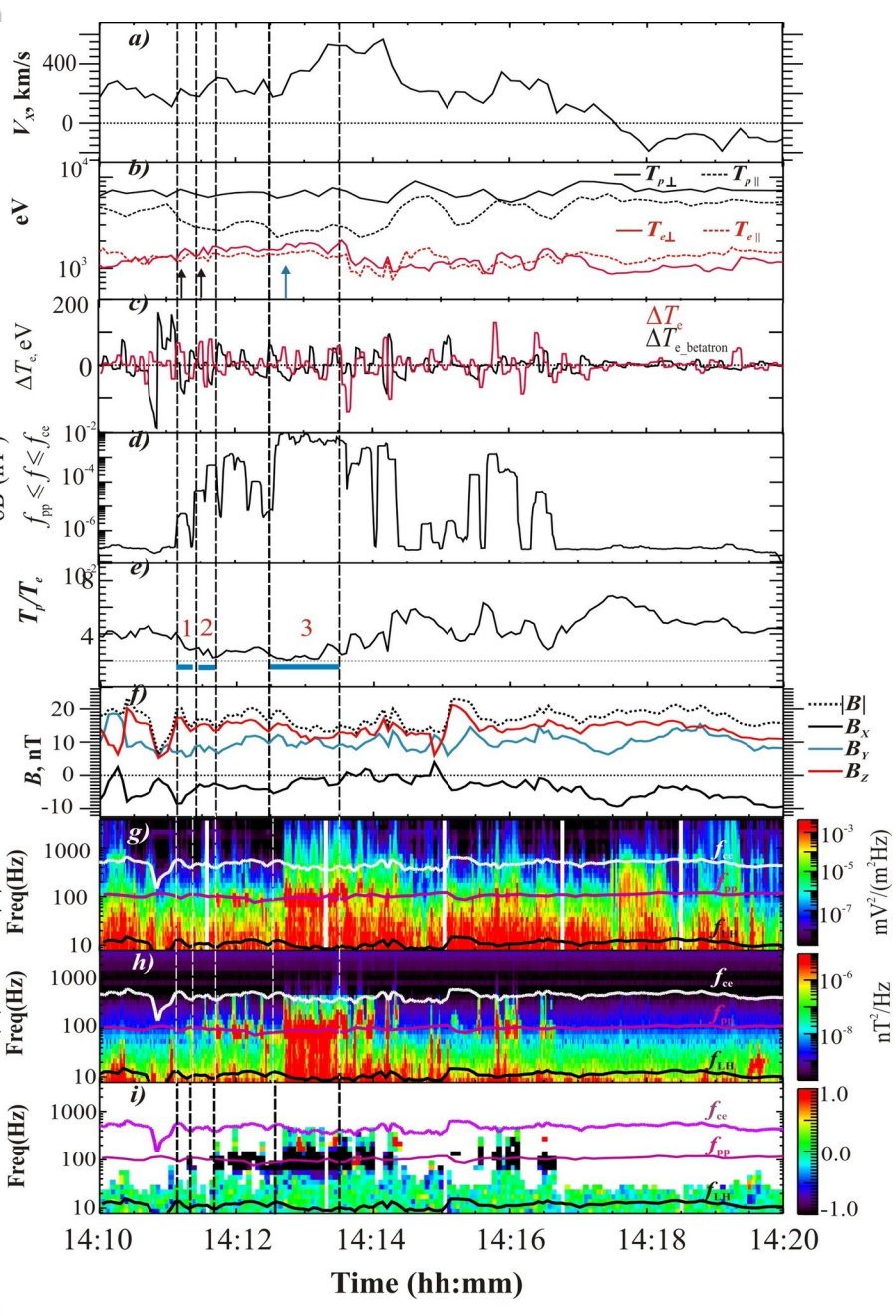

2016JA022874-f04-z-.jpg

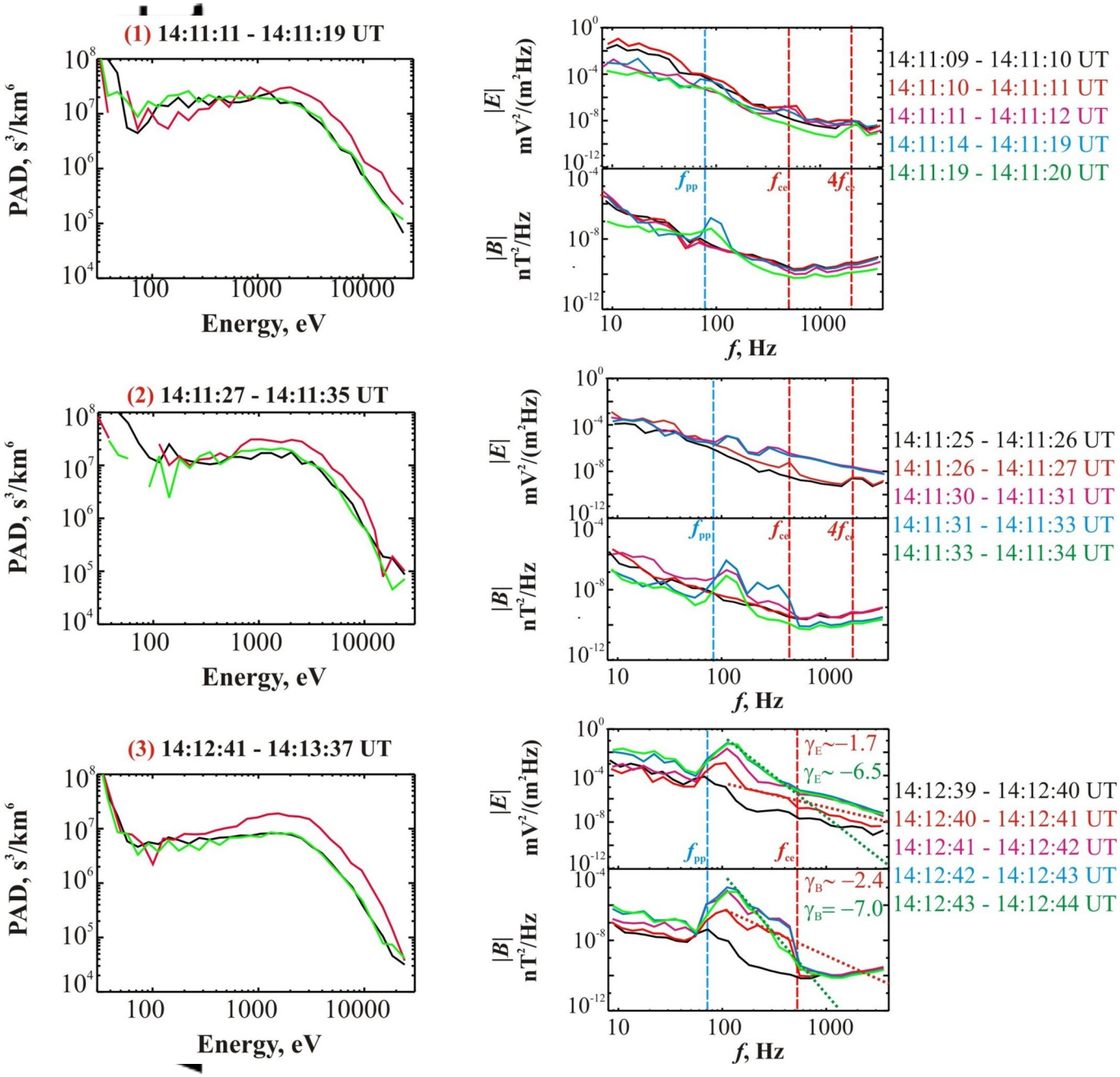

2016JA022874-f05-z-.jpg

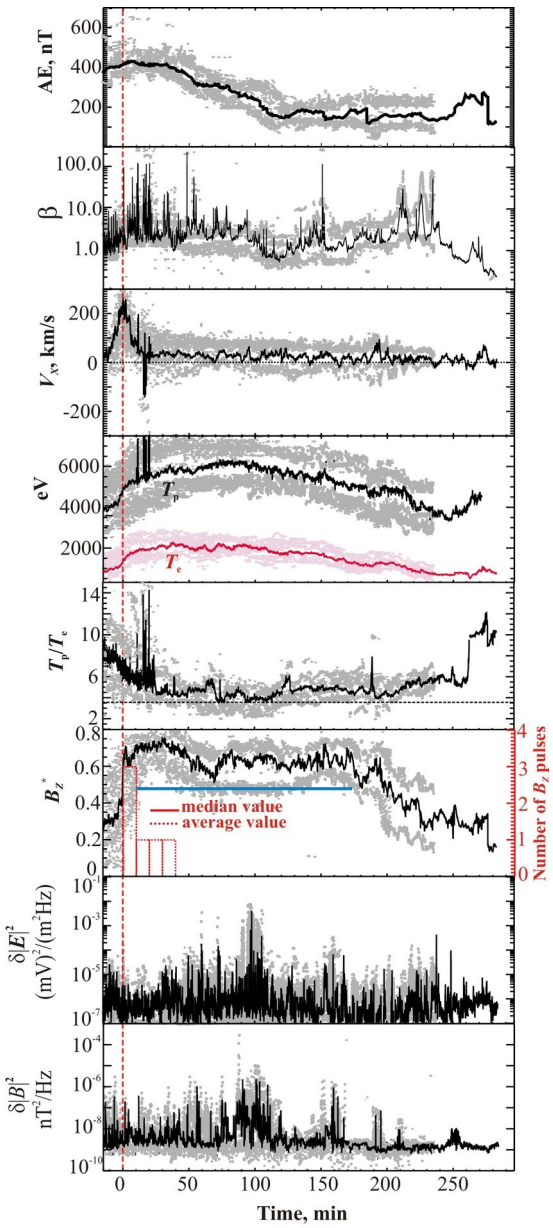

2016JA022874-f06-z-.jpg

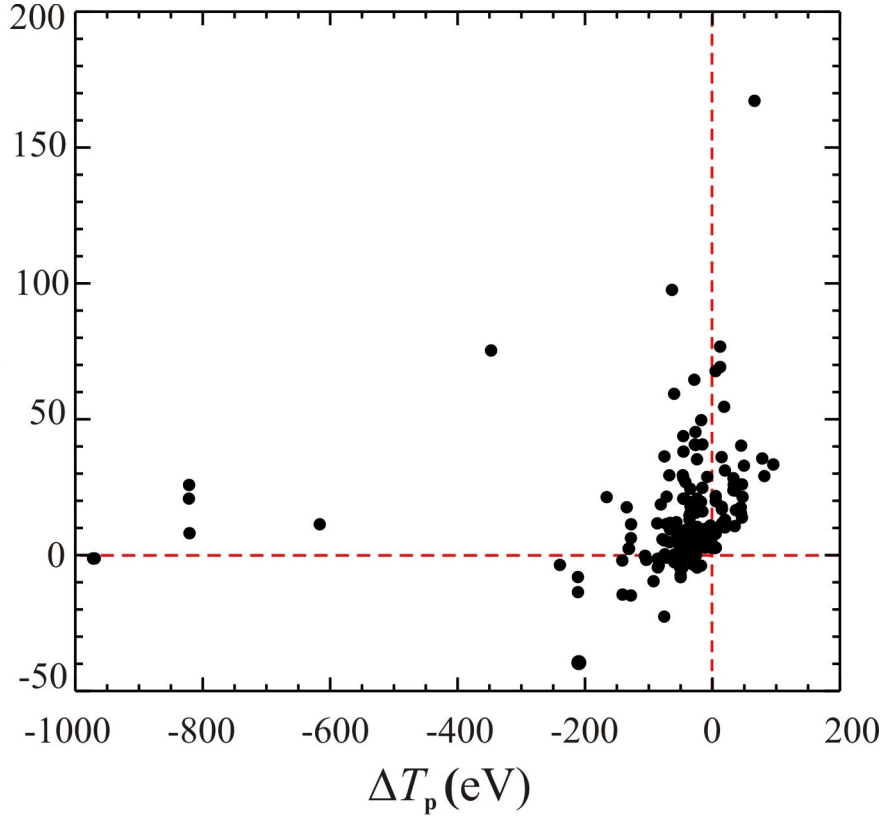

2016JA022874-f07-z-.jpg

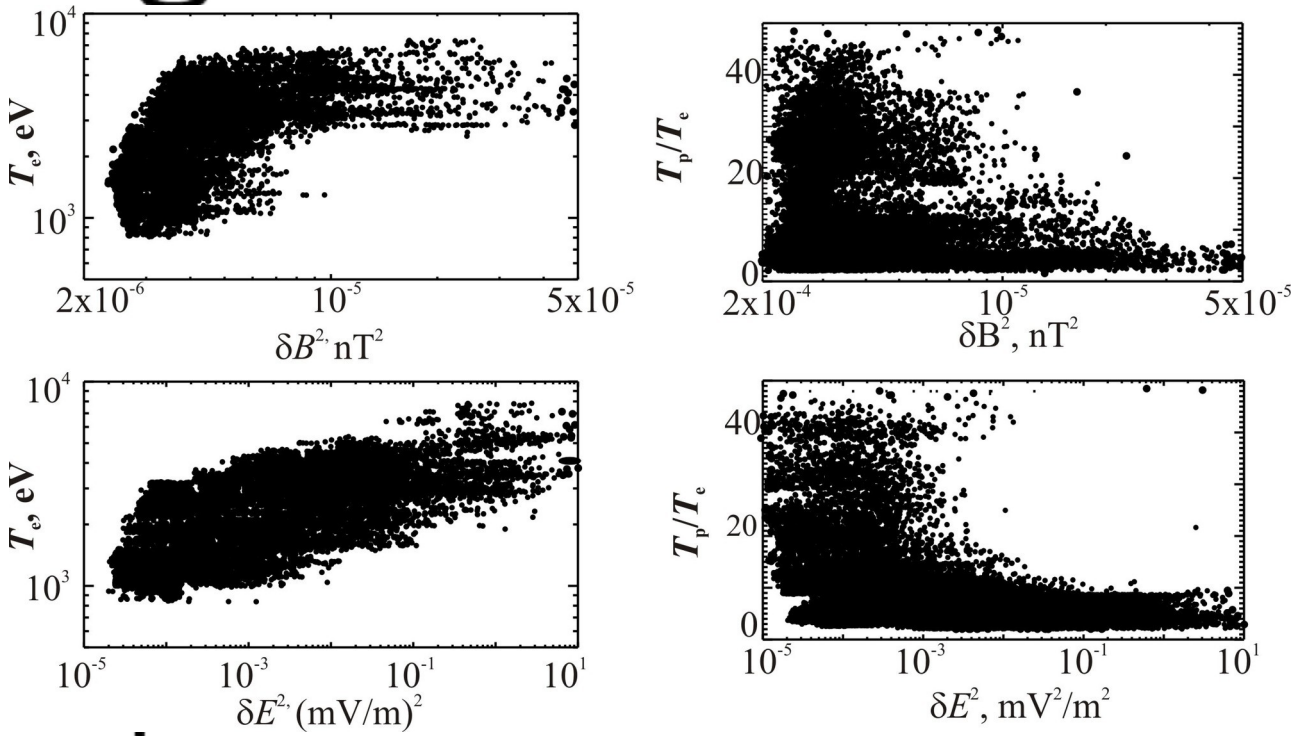

2016JA022874-f08-z-.jpg